ARMY RESEARCH LABORATORY

Experiments and Simulations of Exploding Aluminum Wires: Validation of ALEGRA-MHD

by Robert L. Doney, George B. Vunni, and John H. Niederhaus

ARL-TR-5299 **September 2010**
SAND-2010-6028 P

NOTICES

Disclaimers

Sandia National Laboratories is a multi-program laboratory managed and operated by Sandia Corporation, a wholly owned subsidiary of Lockheed Martin Corporation, for the U.S. Department of Energy's National Nuclear Security Administration under contract DE-AC04-94AL85000.

The findings in this report are not to be construed as an official Department of the Army position unless so designated by other authorized documents.

Citation of manufacturer’s or trade names does not constitute an official endorsement or approval of the use thereof.

Destroy this report when it is no longer needed. Do not return it to the originator.

Army Research Laboratory
Aberdeen Proving Ground, MD 21005-5069

ARL-TR-5299 **September 2010**

SAND-2010-6028 P

Experiments and Simulations of Exploding Aluminum Wires: Validation of ALEGRA-MHD

Robert L. Doney
Weapons and Materials Research Directorate, ARL

George B. Vunni
Bowhead Science & Technology, LLC., Aberdeen, MD

John H. Niederhaus
Sandia National Laboratories, Albuquerque, NM

REPORT DOCUMENTATION PAGE	Form Approved OMB No. 0704-0188

1. REPORT DATE *(DD-MM-YYYY)*	2. REPORT TYPE	3. DATES COVERED (From - To)
September 2010	Final	March 2009–May 2010

4. TITLE AND SUBTITLE
Experiments and Simulations of Exploding Aluminum Wires: Validation of ALEGRA-MHD

5a. CONTRACT NUMBER

5b. GRANT NUMBER

5c. PROGRAM ELEMENT NUMBER

6. AUTHOR(S)
Robert L. Doney, George B. Vunni[*], and John H. Niederhaus[†]

5d. PROJECT NUMBER

5e. TASK NUMBER

5f. WORK UNIT NUMBER

7. PERFORMING ORGANIZATION NAME(S) AND ADDRESS(ES)
U.S. Army Research Laboratory
RDRL-WMP-D
Aberdeen Proving Ground, MD 21005-5069

8. PERFORMING ORGANIZATION REPORT NUMBER
ARL-TR-5299
SAND-2010-6028 P

9. SPONSORING/MONITORING AGENCY NAME(S) AND ADDRESS(ES)

10. SPONSOR/MONITOR'S ACRONYM(S)

11. SPONSOR/MONITOR'S REPORT NUMBER(S)

12. DISTRIBUTION/AVAILABILITY STATEMENT
Approved for public release; distribution is unlimited.

13. SUPPLEMENTARY NOTES
[*]Bowhead Science & Technology LLC., Aberdeen, MD
†Sandia National Laboratories, Albuquerque, NM

14. ABSTRACT
To perform armor simulations with quantifiable confidence, we need to validate material models by comparing a variety of computational data with carefully measured experiments. Exploding wires serve as excellent tests of material models since one can tune the energy deposition so that the wire passes through solid, liquid, and gas phases. The experimental data collected includes electrical measurements where material properties vary over a wide range of temperature, pressures, and electrical conductivities. In this work, we focus on aluminum wires immersed in a water environment. Our simulations show outstanding agreement with experiment when one factors in measurement uncertainty. We find great sensitivity with certain parameters, which lead to large variability in the results at late time.

15. SUBJECT TERMS
ALEGRA, MHD, exploding wires, modeling, plasma, simulation

16. SECURITY CLASSIFICATION OF:			17. LIMITATION OF ABSTRACT	18. NUMBER OF PAGES	19a. NAME OF RESPONSIBLE PERSON
a. REPORT	b. ABSTRACT	c. THIS PAGE			Robert L. Doney
Unclassified	Unclassified	Unclassified	UU	58	19b. TELEPHONE NUMBER (*Include area code*) (410) 278-7309

Standard Form 298 (Rev. 8/98)
Prescribed by ANSI Std. Z39.18

Contents

List of Figures

List of Tables

Acknowledgements

The authors gratefully acknowledge several individuals who have helped us make this study possible. Specifically, we are indebted to Dr. John Powell and Dr. Dan Hornbaker for their critical review of this manuscript; Dr. Alan DeSilva for providing facilities to perform the experiments; Mr. Eric Klier for providing SEM images of the wire; Dr. Mike Desjarlais, Dr. Kyle Cochrane, Dr. Erik Strack, and the rest of the ALEGRA development team for their interest, technical support, and helpful discussions along the way. We would also like to thank the Distributed Shared Resources Center, part of the DoD High Performance Computing Modernization Program, located at the Aberdeen Proving Grounds for access to the computational resources.

INTENTIONALLY LEFT BLANK.

1. Introduction

The dynamics of a metallic, exploding wire (EW) contains rich and interesting physics. A large amount of study through the 1960s has been compiled in the four-volume workshops on the subject (*1*–*4*). Chace (*5*) provides an interesting EW history dating back as far as 1773 to Nairne as well as identifying applications such as detonating explosives (referred to as bridge wires) and photographic light sources, for example. One area that has been the subject of much research is the expansion rate of EW and its relationship to the rate of energy deposition (*6, 7*). For example, Sinars et al. (*8*) shows that for a variety of wire materials, the (wire core) expansion rates are related to energy deposition prior to plasma formation around the wire.

Exploding wires also provide a means to investigate fundamental physics. One may adjust the wire radius and externally applied voltage so that the wire passes through solid, liquid, and gas phases. Consequently, EW is an ideal problem for validation of hydrodynamic codes and material models. As Rosenthal and Desjarlais point out, ". . .the importance of good exploding wire data cannot be overstated. Experimental details of the exploding wire evolution provide both qualitative (voltage collapse) and quantitative (time of voltage collapse, peak voltage, and core expansion rate) features that simulations must match if they are to be considered accurate." (*9*)

A number of recent experimental and computational studies have been undertaken on EW to address validation. However, magnetohydrodynamics (MHD) simulations of EW reported in the literature show wide variations, depending on the simulation code, material models, and conductivity models used (*10, 11*). Mehlhorn et al. (*12*) reported the first validation of the two dimensional ALEGRA-MHD code using bare wires, wires with insulating coatings, and tamped—or confined—wires. They reported good agreement between simulation and experiments for only confined wire explosions, suggesting recent improvement in the equations of state (EOS) and conductivity models. In a series of papers using one-dimensional ALEGRA simulations, Sarkisov et al. (*13*), reported the dependencies measured in electrical exploding wires over the entire range of the heating rates. Their simulations showed that both the melting and volume vaporization begin close to some equilibrium phase boundaries even at the maximal heating rates. They further demonstrated separation of the exploding wire into a high-density cold core and a low-density hot corona as well as fast rejection of the current from the wire core to the corona during voltage collapse.

In this document we are interested in comparing experimental and computational simulations of an exploding aluminum (Al) wire. Our validation approach is similar to the work reported by Mehlhorn et al., who showed regions where the simulation and experimental results agree, and demonstrates the accuracy of the material models, conductivity models, and EOS.

This work expands previous EW validation studies by examining and incorporating the uncertainty of many experimental parameters. Practical validation is not complete without including such a fundamental reality prevalent in all experimental work. More specifically, a direct comparison of experimental and numerical data that excludes uncertainty may lead to an entirely different conclusion because a 1% change in some variable—a completely reasonable amount—may have huge consequences at later times. Without performing the requisite analysis, however, this can easily be missed and divergences at late time could mistakenly be blamed on computational material models. Until recently, access to computational resources was not sufficiently available to address the large number of parameters—and the number of variations per parameter at the appropriate resolutions—for this problem in its two-dimensional (2D) form. The present study takes advantage of powerful computational resources to investigate the effect of uncertainty in parameters governing the EW system.

The report is organized as follows. In section 2, we provide details of the experimental setup. In section 3, we describe the computational setup including material models, boundary conditions and tests of parameter sensitivity. In section 4, we compare and discuss the experimental and computational results, with conclusions given in section 5.

2. Experimental Setup

Three sets of experiments were performed with stainless steel electrodes and Al wire (of 99.95% purity) supplied by Goodfellow Inc. Bulk wound wire for these experiments was supplied with a specified diameter of 0.125 mm ±10%. A typical analysis of the purity reported by the manufacturer indicated: Cu<500, Fe<4000, Mn<500, Si<3000, Zn<1000 parts per million by weight. Table 1 shows the mean RLC circuit and wire parameters for each experimental run. The circuit parameters in table 1 represent the values for the circuit components external to the EW apparatus.

Table 1. Experimental parameters with estimated uncertainty.

Voltage (kV)	19.98
Inductance (μH)	1.15
Resistance (Ω)	2.00 ± 0.10
Wire length (mm)	16.5 ± 5%
Wire diameter (μm)	126.26 ± 1.89

Exploding wire physics is extremely sensitive to wire radius, so the 10% tolerance provided by the manufacturer was insufficiently precise for this work (see figure 12 for example). To better

characterize this uncertainty, several positions along a specimen were imaged using scanning electron microscopy (SEM). Figure 1 shows one of these images, with spatial scale included. From these measurements, the mean wire diameter listed in table 1 was obtained.

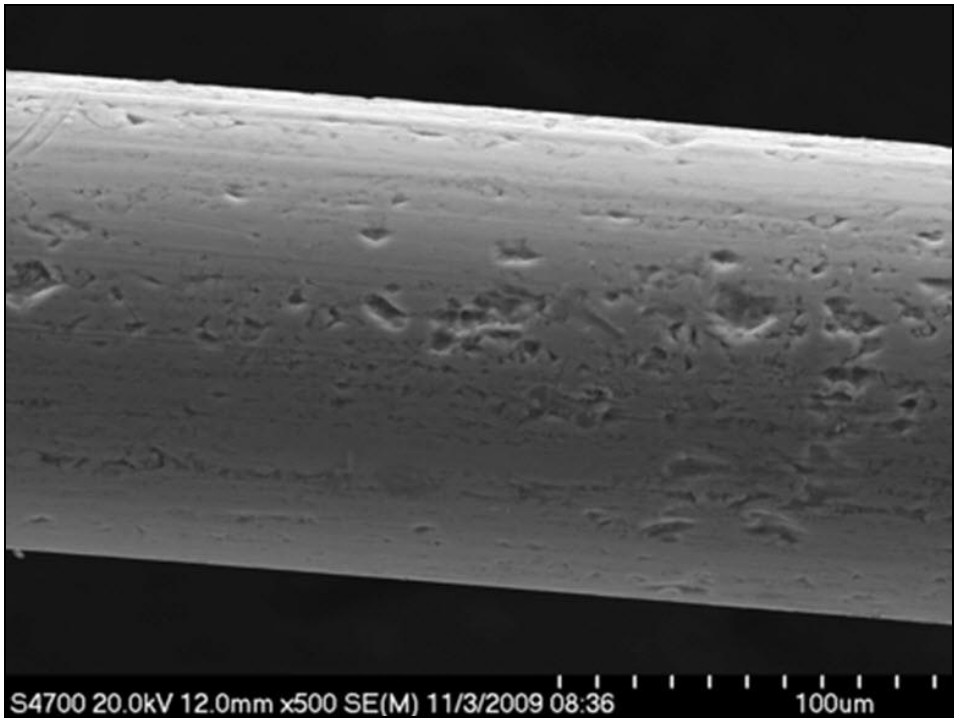

Figure 1. SEM image of an Al wire used in this study.

The experimental setup consisted of a cylindrical Al chamber 15-cm deep and 30-cm in diameter. Details of the experimental apparatus have been reported in our previous publications (*14–16*). In the previous experiments, we assumed the length of the wire to be equal to the plate separation. However, during the parameter sensitivity study—outlined in section 3.7—we discovered that the current trace was surprisingly sensitive to uncertainties in wire length after peak current. Therefore, the specifics of the wire attachment are described as follows. The wire was fed through a hole between an active electrode in the center of the chamber and a return electrode above. One small lead fishing sinker (sphere) was forced into each cathode and anode opening such that its edge aligned—within measurement error—to the electrodes inner edges. Therefore the assumption that wire length was equal to the plate separation was not accurate enough. We estimate this error to be approximately 5%, just under 1 mm, of the actual length as reported in table 1.

The wire is rapidly heated and vaporized by current switched into it from a 1.88 μF capacitor, which was charged to an initial voltage up to 20 kV. Measurement revealed this to be 19.98 kV. The overall circuit setup has an inductance of 1.15 μH and resistance of 2.0 Ω. Vaporization occurs in approximately 1 μs. As the plasma expands, distilled water confines the expansion so that, to close approximation, a cylindrical plasma column forms, which is uniform everywhere

except near the electrodes. In previous work, it was observed that the plasma uniformity can be maintained with the use of a distilled water bath, since the sound speed within the plasma is greater than the boundary expansion speed. Therefore, conditions inside reach equilibrium more rapidly than in the case where wire expansion takes place in vacuum or air (*17*).

The voltage across the wire is measured with a 670:1 high-voltage resistive divider, followed further by a 25:1 divider at the recording digital oscilloscope and a correction made in the software for the small reactive component of the voltage. Current is measured with a Rogowski loop surrounding the active electrode inside the chamber, where the output is passively integrated with an RC integrator, and corrected in the analysis software for the RC decay time. The rate of expansion of the plasma column is recorded with the aid of a rotating mirror streak camera. The plasma is backlit by a xenon flashlamp and imaged on a narrow slit, with the plasma axis perpendicular to the slit. The light passing through the slit represents a thin slice across the column diameter about midway between the electrodes. Light from the slit passes to a rapidly rotating mirror and is then focused on an intensified digital camera. The result is a silhouette displaying the time history of the plasma column diameter (which is discussed in section 4).

The primary recorded data are the voltage and current at 4-ns intervals, and the column diameter measured from the streak image. The streak images are digitized to give column diameter as a function of time, and measurements from the images are interpolated to produce a table of plasma diameters at the same 4-ns intervals. The current, voltage, and diameter data are input into an analysis program that steps through these data, tracking the development of column diameter, density, and internal energy. The column resistance R at each step is simply obtained from Ohm's law as $R = V/i$, and the conductivity is obtained from $\sigma = \ell/RA$, where A is the instantaneous cross-sectional area of the column and ℓ is its length, which is constant due to the massive electrodes. The experimental measurements of the voltage and current are quite reproducible, but may have some potential errors. Quantities whose measurement in the experiment may incorporate significant uncertainty include—but are not limited to—capacitor voltage, circuit resistance and inductance, wire dimensions (radius and length), discharge timing, and spatial and temporal scale factors used in digitizing the streak image.

The error in the measured circuit voltage, inductance and resistance traces is estimated to be approximately 2%. Errors in the wire dimensions may also manifest themselves in these traces. For example, an error in the column radius is reflected in both the density and conductivity, correlated in such a manner that a positive error in radius produces a reduction in both computed density and conductivity, and vice versa.

3. Computational Setup

3.1 Description of ALEGRA

The finite-element MHD code ALEGRA is employed here for simulating the EW experiments. ALEGRA was originally developed to provide computational support for Sandia National Laboratories (SNL) wire initiation and Z-pinch collapse investigation efforts (*18–21*). It couples Maxwell's equations with multimaterial solid dynamics in the MHD approximation, which ignores displacement currents (*22, 23*). ALEGRA incorporates magnetic forces by computing the local Maxwell stress and adding it to the stress tensor appearing in the finite element formulation. The constrained transport method is used to remap the magnetic flux in the Lagrange-remap formulation. Resistive diffusion of the magnetic field—and the associated Joule heating of the medium—is treated in the code by use of an implicit parallelized linear-solve operation for the transient magnetic diffusion problem, using tabulated electrical conductivity (EC) data for the simulated materials.

3.2 Overview

Our computational domain is described by a 2D, axisymmetric, Eulerian mesh with unit aspect-ratio (square) elements. Figure 2 illustrates the simulation geometry, including the connecting anode and cathode plates, wire, and water environment. The radial direction is horizontal and the *z*-axis is vertical. We avoided biased meshes here because of inherent limitations in the accuracy of the magnetic diffusion solve operations for elements with an aspect ratio far from unity. Semi-empirical, SESAME EOS tables with the Lee-More-Desjarlais (LMD) EC (*24*) models were used in the simulations.

The plates were included explicitly in the simulations because their electrical connection to the wire is physically relevant, owing to the development of current concentrations and regions of intense, localized resistive heating near the contact. Material in these regions may experience phase changes sooner than wire material far from the plates. Thus, for this degree of realism, we must simulate the problem with a minimum of two spatial dimensions. It is important to note that for computational efficiency, the full radius of the electrodes and water bath are not included in the domain. We typically make the radial extent of the computational domain only as large as it needs to be—capturing the relevant magnetic field so that the correct, or converged, inductance is obtained thus leading to the proper current in the conductor. Larger meshes add unnecessary computational cost to each simulation. This will be quantified in section 3.5.

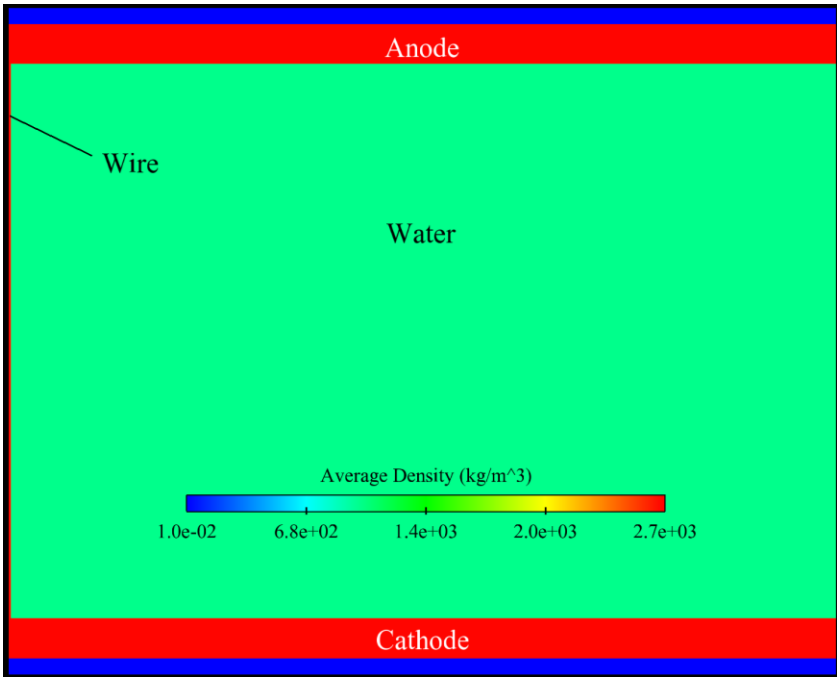

Figure 2. Full domain, half symmetry of the initial state of a typical exploding wire simulation setup.

3.3 Boundary Conditions

MHD simulations in ALEGRA may be driven by specifying a current density or magnetic flux density field on the boundaries, or in source terms. Here, we take advantage of the feature that allows the boundary fields to be determined by a time-dependent circuit model. A coupled circuit solver is used to compute circuit behavior in each timestep, where the circuit is represented by a node network and lumped circuit parameters. The code treats the mesh as a single circuit component, with dynamic inductance and resistance computed in each timestep as lumped parameters.

For this problem, current is intended to flow into the mesh through the anode, down the wire, and back out of the mesh through the cathode. However, the direction of the current is actually arbitrary. Ampère's law for an infinite current-carrying wire governs the magnetic field magnitude:

$$B = \left(\frac{\mu_0 i}{2\pi R^2}\right) r \qquad \text{inside the wire } (r<R) \tag{1}$$

$$B = \frac{\mu_0 i}{2\pi r} \qquad \text{outside the wire } (r \geq R) \tag{2}$$

where i is the current, B is the magnetic field strength at r, μ_0 is the permeability of free space, R is the wire radius, and r is the radius where the field is measured. For current flowing along the axis, the field is oriented azimuthally about the wire. Inside the wire, the field must decay to zero on the axis.

The boundary conditions (BC) for this problem, therefore, require zero magnetic field along the axis of symmetry, where r=0 (equation 1 and left edge of figure 2). At the right edge of figure 2, differing BCs are required along the vertical. For example, Ampère's law governs the field between the conducting plates as described by equation 2, while magnetic diffusion must be allowed to produce the field in the plates naturally. The BCs can therefore be applied based upon the material that is in contact with the edge. This is accomplished using a "material mask" in ALEGRA. With the magnetic field thus imposed, the total current i arises on the conductors. Zero-field conditions are maintained naturally through the MHD finite-element formulation on the axial boundaries and at the top and bottom of the figure—since the air outside the plates is not expected to carry any magnetic field. These constraints are all coupled into the problem using the "cylindrical radial slot," "centerline," and "E tangent" boundary conditions implemented in ALEGRA (*19*).

3.4 Material Models

Many various tabulated Al EOS models are available within ALEGRA. We investigated the following SESAME tables for Al using the (standard) Kerley interface to the tables: 3700, 3711, 3720, and 3721. We also included the ANEOS model 4020 for the Al 2024 alloy to demonstrate the necessity of separate models for alloys. Several models for aluminum's electrical conductivity are also available in ALEGRA, which are discussed and investigated in following sections. For water, two SESAME tables are available: 7150 and the more recent 9150. We found the current and resistance traces to be almost identical regardless of the water EOS. Water conductivity however, plays a major role as section 3.7.6 emphasizes.

3.5 Computational Mesh Convergence

Simulations require both adequate spatial resolution and spatial extent in order to ensure convergence of the solution. If the mesh resolution is too coarse, numerical truncation error may become significant, and physically important features may not be resolved. If the mesh does not extend to a great enough radius, significant magnetic energy—and the associated inductance—may be lost. Hence, error in the load inductance would propagate to the circuit response time, Joule heating rates in the mesh, and ultimately the timing of wire expansion.

One can use inductance in the mesh as a measure for adequate spatial extent of the mesh. Here, we extract the steady-state value of inductance as a function of mesh size using a very small driving voltage. Figure 3 plots the inductance as a function of time for several cases where the radial extent increases from 100 to 700 wire radii (R_w).

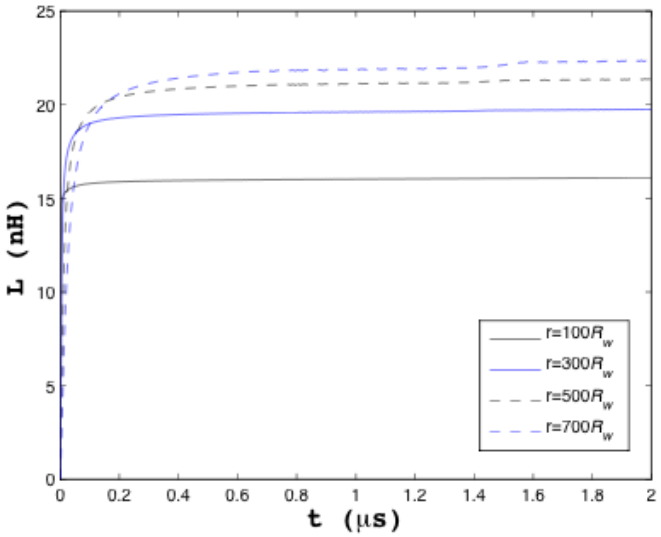

Figure 3. Load inductance as a function of time for low-voltage simulations.

Our full exploding wire simulations are only run for 6 μs; from the figure it is clear that the inductance has reached a near-steady-state value by 2 μs, and that the final value exhibits an asymptotic trend as the radial extent of the mesh increases. For the case of r=700 R_w, it is unclear what causes the inductance to increase by about 1% at 1.55 μs. We assume that even at low driving voltage, and even after several magnetic diffusion times, the current distribution in the wire interior may change in time since the conductivity is not fixed. Nonetheless, we use the inductance recorded at 2 μs to monitor sufficient radial extent of the mesh.

Figure 4 illustrates the low-voltage, steady-state inductance at t=2 μs as a function of the radial extent of the mesh in multiples of the wire radius, R_w.

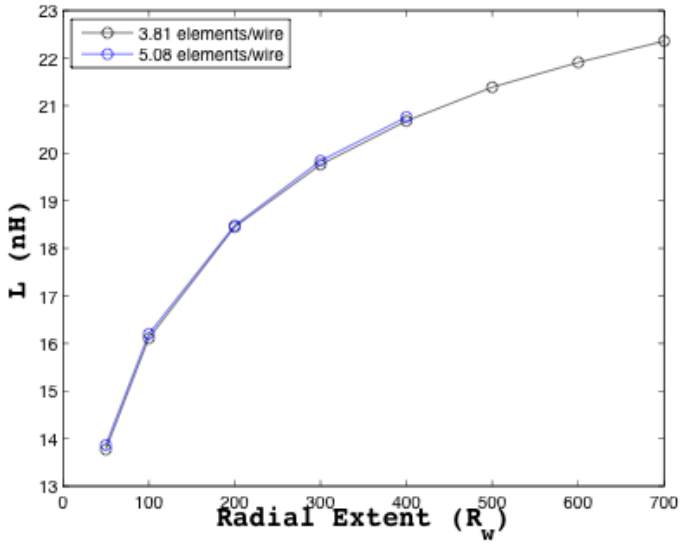

Figure 4. Load inductance as a function of radial mesh extent for low-voltage simulations.

The black data series measures this for a resolution of 3.81 elements across the wire radius. It was unclear if there were correlations between the resolution and radial extent of the mesh so we also performed calculations with 5.08 elements across the wire (blue data series). Based on these results we conclude that a radial extent of the mesh equal to 500 times the wire radius has a sufficiently converged inductance. The change to 600 R_w is on the order of a few percent based on a total inductance of about 21.5 nH, which has negligible impact on the current trace (not pictured) but a significant impact on total simulation time. Further, increasing the resolution to 5.08 elements across the wire radius has a negligible impact and so we posit that 3.81 elements are sufficient.

The simulation inductance of 21.5 nH is in excellent agreement with a simple analytical estimate. The inductance due to current in the wire, in the dc limit (fully diffused field) is given by Knoepfel in equation A1.3 (*25*) as

$$L_W = \frac{\mu_0 \ell}{2\pi}\left[\ln\left(\frac{2\ell}{R_W}\right) - \frac{3}{4}\right], \tag{3}$$

where ℓ=1.65 cm is the length and R_W=63.13 μm is the radius of wire. Inserting values of ℓ and R_W, the inductance due to current in the wire is L_W=18.2 nH. Meanwhile, the inductance due to current in the two parallel circular plates is approximated using the expression for inductance in rectangular plates:

$$L_p = \frac{\mu_0 A_f}{w} = \frac{\mu_0 r_p d_p}{2\pi r_p} = \frac{\mu_0 d_p}{2\pi}$$

where A_f is the area enclosing the magnetic flux between the plates, w is the dimension transverse to the current, d_p=1.65 cm is the distance between the plates, and r_p=3.16 cm is the effective radius of the plates in the simulation with radial extent 500 R_W. Evaluating this expression, we found the inductance of the two plates to be approximately L_p=3.3 nH. Hence, the total inductance of the system (plate and wire) is approximately 21.5 nH, which agrees with the simulation result for 500 R_W.

Up to this point we have considered the wire to be the smallest object to resolve and only measured inductance out to 2 μs with a very small voltage. We were concerned that the wire-water interface might be mesh sensitive at later times when the full voltage was considered. To check for resolution convergence over the full EW simulation, figure 5 superimposes the current traces with varying resolutions—1.27, 2.54, 3.81, and 5.08 elements across the wire radius—for constant radial extent of the mesh (400 R_w). Traces for the last two resolutions overlap. Again, it is clear that results have converged for 3.81 elements across the wire radius, and this holds true during the process of wire explosion and current recovery.

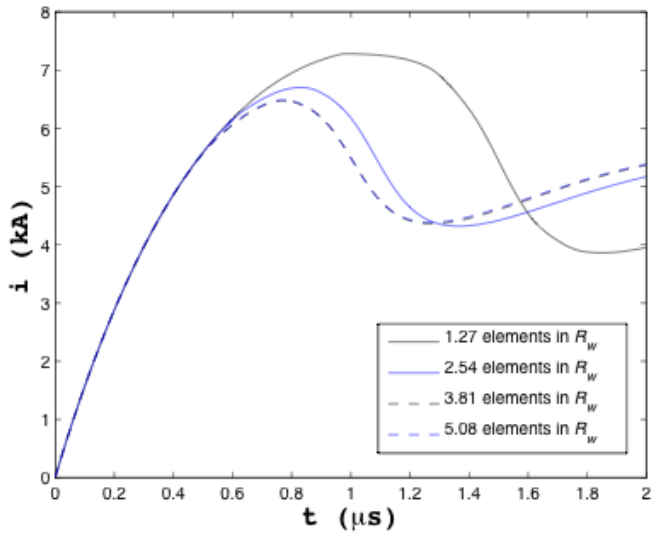

Figure 5. Current as a function of time for several mesh resolutions, at 400 R_W.

3.6 Overview of Circuit Behavior

The behavior of the circuit in EW systems has been very well characterized in the literature. For the present study, we recognize three periods in the time evolution of the simulated current and voltage, corresponding to the different phases of the wire material: solid, liquid, and vapor. These phases can be recognized in figure 6. The simulated internal energy of the wire material is plotted using the left-hand scale. Also shown using this scale are horizontal red lines indicating the estimated energy required for melt (0.576 J) and vaporization (8.01 J), based on tabulated values of the specific heat and latent heat of fusion and vaporization for aluminum. Thus the

time at which the internal energy is equal to melt is approximately when the voltage (or similarly, wire resistance) suddenly jumps after a brief thermal expansion phase around 0.5 μs. We expect that the connection to the wire via plates will be interrupted due to localized resistive heating before the wire can vaporize. This is likely a strong contributor to what limits the current. At some time between current maximum and voltage maximum, the amount of internal energy reaches that which is required for vaporization—note the unsmooth ramp just preceding voltage max. The wire explodes as the voltage peaks. Consequently, the current drops further. As the expanding plasma heats due to residual current, conditions are favorable to establish a conductive path. At later times, current peaks again but then falls off with voltage. Deposited energy saturates as negligible current is conducted across the plates.

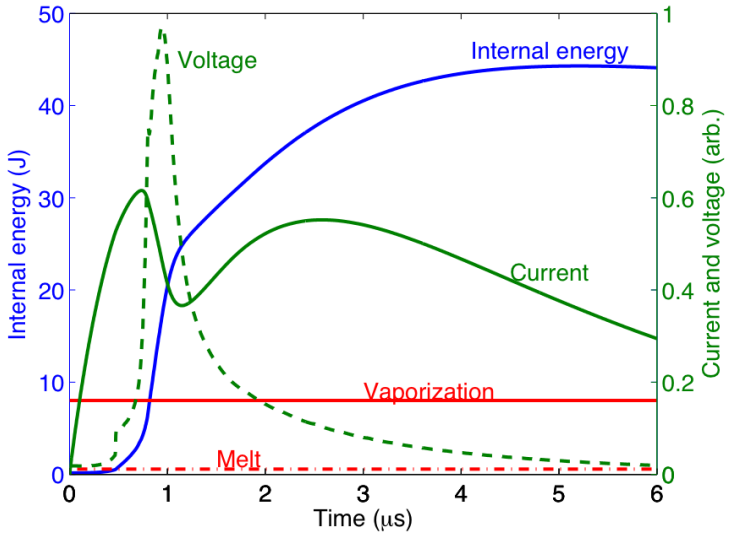

Figure 6. Normalized histories of current and voltage for the present EW system, with wire internal energy. Horizontal red lines indicate estimated energies for phase changes.

The most important features of the simulated circuit histories shown in figure 6 are the maximum and "local minimum" points of the current trace, and the single maximum in the voltage trace. These features appear in all of the simulations discussed here (except in the case where water conductivity is artificially increased). The current maximum slightly precedes the voltage maximum. The local minimum in current follows the voltage maximum as the voltage collapses. The data shown here suggest that the wire is, mostly likely, entirely in the vapor phase at the onset of voltage collapse; however, the displayed phase changes do not consider any corrections due to superheating.

3.7 Parameter Sensitivity

In this section, we address uncertainties and parameter sensitivities expected to be present in these calculations. Specifically, we look at how the current trace is perturbed by processor scaling; uncertainty in external circuit parameters and wire dimensions; variations in the plate or

electrode thickness; and the choice of a water conductivity model. We chose the current trace as a metric as it affects the changing thermodynamic state of the material via the conductivity. We also chose to use the SESAME 3700 EOS table for Al in these parameter sensitivity studies since it is the recommended table in the ALEGRA Kerley EOS interface. In general, for all of these variations we found that the current trace was mostly unchanged through peak current. This is consistent with observations by Baker (*26*) that, up until burst, wire inhomogeneities are not important. As the current decayed towards a local minimum, diverging results indicated a greater impact of parameter sensitivity. The results would then converge again after the second current maximum. We will discuss this further in section 4. Conclusions of the sensitivity tests in this section should be applicable to a broad variety of exploding wire problems, irrespective of wire material.

3.7.1 Scalability

We tested a sample calculation on 64, 128, 256, and 512 cores. The electrical traces (as well as the timesteps) were virtually identical as figure 7 illustrates. Thus inconsistencies due to parallelism in the simulation results can be eliminated.

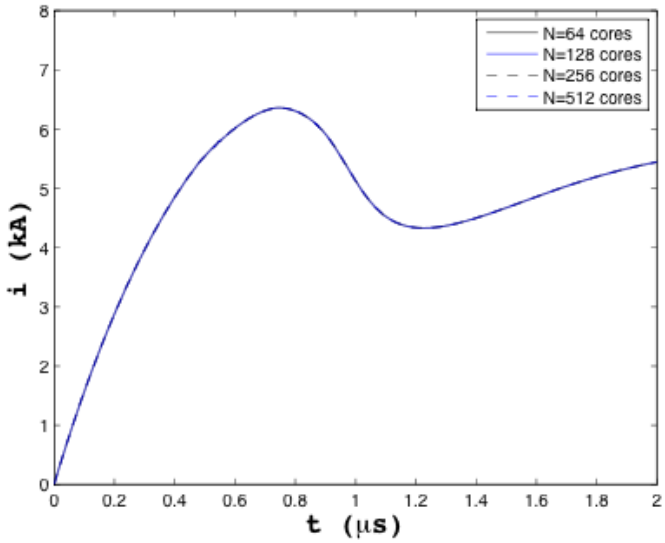

Figure 7. Current as a function of time for a sample simulation testing parallel scalability.

3.7.2 Fracture

We anticipated that fracture would play a negligible role due to the fast energy deposition. Figure 8 confirms this expectation, in terms of the circuit behavior. The current trace is nearly invariant against changes in the simulated fracture strength down to 0.75 GPa, with respect to the case with infinite fracture strength (baseline). There are three cases where fracture is considered using the Johnson-Cook fracture model with standard parameters for aluminum. We chose a baseline fracture strength of 1.5 GPa—a typical value that encompasses many of the Al alloys,

based on ALEGRA repository material data and Davison & Graham (*27*). We then doubled and halved the value to test sensitivity. As the fracture strength increases, the current trace approaches the limiting case of infinite fracture strength.

To introduce greater potential for localized failure, and to account for impurities, we also included a random density perturbation of 0.05% with an aggregate size much smaller (0.02×) than the cell size. Even with this density perturbation, no significant change in behavior is observed. It is likely that fracture will play a larger role for slower energy deposition. This could be accomplished through several means: increased wire radii, lower voltages, and/or higher inductances for example. It is important to note that the density perturbation imposed here is contrived, because the forced symmetry creates annular rings of density variation rather than unique sites. Given the surface roughness as depicted in figure 1, we would like to look into this in a future three-dimensional (3D) study. It should be noted that we believe an impurity's conductivity, rather than its density, will be dominant (for small perturbations).

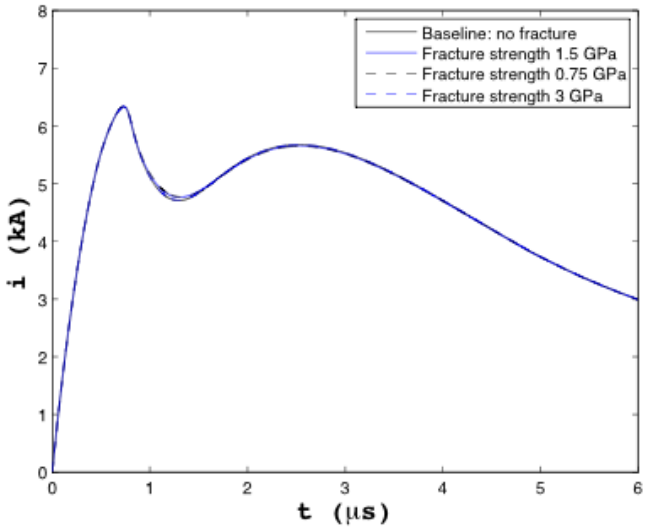

Figure 8. Role of fracture in the current trace for simulation with density perturbation.

3.7.3 Errors in External Circuit Parameters

We found that results were generally stable against uncertainties in the external circuit parameters of a magnitude typically encountered experimentally. In some cases, we looked at larger errors out of curiosity. These include errors of 10% in the capacitor-bank voltage and 2% in the external (non-load) inductance and resistance. Figure 9 illustrates the current as a function of time for a baseline simulation and one that includes a voltage error of -10%. Here we see that variations are manifested chiefly at late times after voltage collapse—when the wire is in the gas phase—but that these variations are relatively small.

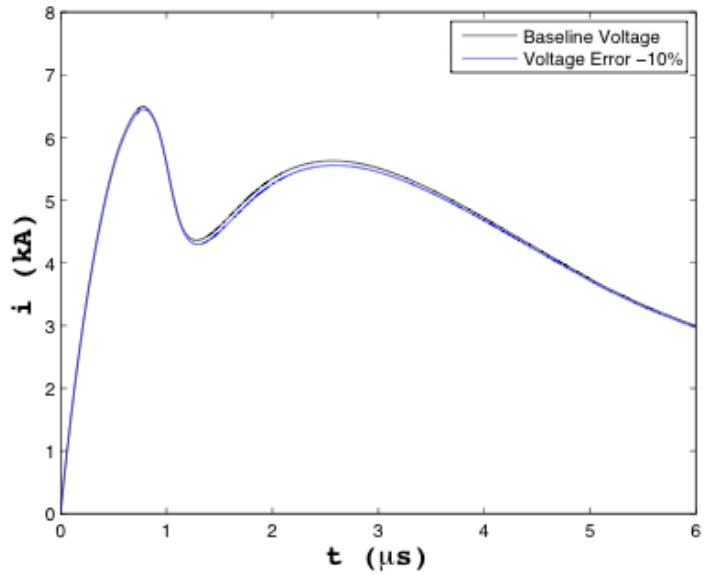

Figure 9. Current trace as a function of time for sample simulation and maximum error of 10% in voltage.

Figure 10 highlights the current as a function of time for a sample simulation with a ±2% error in the external inductance. These results can also be compared with the mesh convergence studies in section 3.5. Note that the current trace is affected much earlier in time as expected because of the influence of the inductance on the current rate di/dt. We are therefore cautious about adding any uncertainty in inductance.

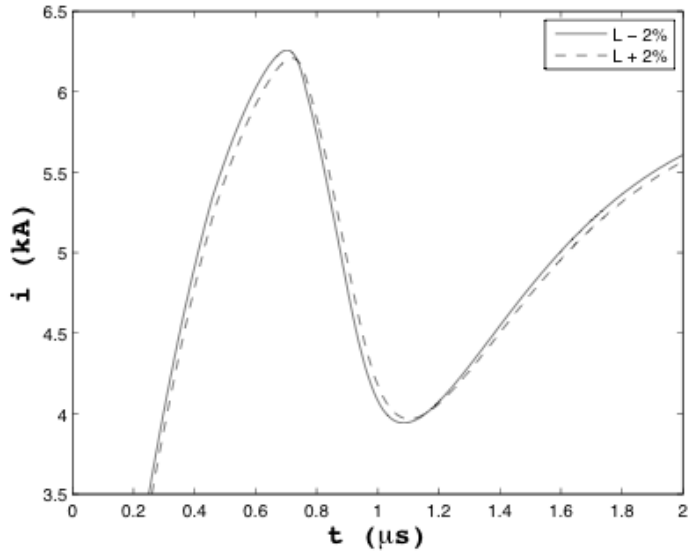

Figure 10. Current as a function of time for a sample simulation with a ±2% error in the external inductance.

Figure 11 highlights the current as a function of time for a sample simulation with a ±2% uncertainty in the external resistance. Here we see that the results are quite sensitive to small errors, particularly at the second current maximum. Additionally, we believe this small uncertainty is quite conservative for commercially available resistors.

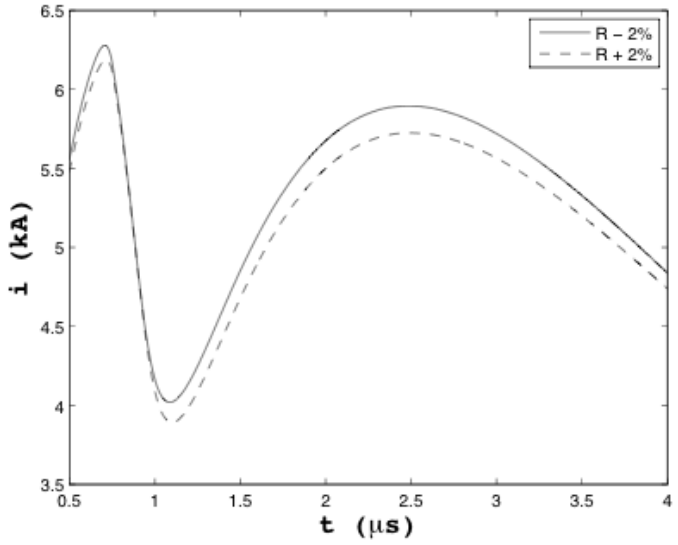

Figure 11. Current as a function of time for a sample simulation with a ±2% error in the resistance.

3.7.4 Error in Initial Wire Radius and Length Measurement

We examined 1–2% errors in the wire radius (figure 12) and a 1% error in its length (figure 13). In the former, a 1% error (black solid and dashed lines) bounded large regions beyond peak current. It is not surprising that the current trace is sensitive to wire radius. The time taken to heat a metal rod up to melt temperature with a constant current *i* is proportional to r^4/i^2, which is obtained from the following argument. The time rate of change of thermal energy density *Q* in a solid conductor of material density ρ, carrying current density *J* is equal to the Joule heating rate:

$$\frac{dQ}{dt} = \frac{1}{\sigma} J^2 , \tag{4}$$

where $Q = \rho C_v T$, C_v is the specific heat at constant volume, *T* is temperature, and σ is the electrical conductivity. The contribution from thermal conduction is ignored here, because of the much longer timescales on which conduction operates (see section 3.7.2). Up to melt, C_v is approximately constant, and for constant electrical conductivity, equation 4 becomes

$$\rho C_v \Delta T = \frac{1}{\sigma} \int_0^t J^2 dt , \tag{5}$$

with $i = JA = J\pi r^2$, this can be solved for t_m, which is the melt time:

$$t_m = \rho C_v \Delta T \pi^2 \sigma \left(\frac{r^4}{i^2} \right). \tag{6}$$

A similar argument could be applied to calculate the vaporization time. Hornbaker (*28*) points out that a more sophisticated form can take into account the approximately linear increase in wire resistivity with temperature. The resistivity can be written as $\sigma^{-1} = \sigma_0^{-1}\left[1 + a\Delta T\right]$ where a is the coefficient of electrical resistivity (about 0.0043 for Al). Bringing σ back into the integrand and rewriting equation 5 we obtain,

$$\Delta T = \frac{J^2}{\rho C_v \sigma_0} \int_0^t \left[1 + a\Delta T\right] dt$$

This equation can be recast as a first order linear differential equation, $d(\Delta T)/dt - Ga(\Delta T) = G$, where $G = J^2/\rho C_v \sigma_0$, and the solution can be obtained by an integrating factor. Evaluating this differential, the solution takes the form,

$$t_m = \frac{\rho C_v \pi^2 \sigma_0}{a} \left(\frac{r^4}{i^2} \right) \ln\left(a\Delta T + 1\right)$$

As this and equation 6 indicate, slight changes in wire radius can significantly impact the times to melt and, consequently, vaporization.

The wire length ℓ also influences the current trace, though not as strongly as wire radius. Length acts primarily via the inductance, as indicated in equation 3. Results for varying the wire length are shown for a subregion of the current history in figure 13 (note that in the image, the wire length is denoted as L_w).

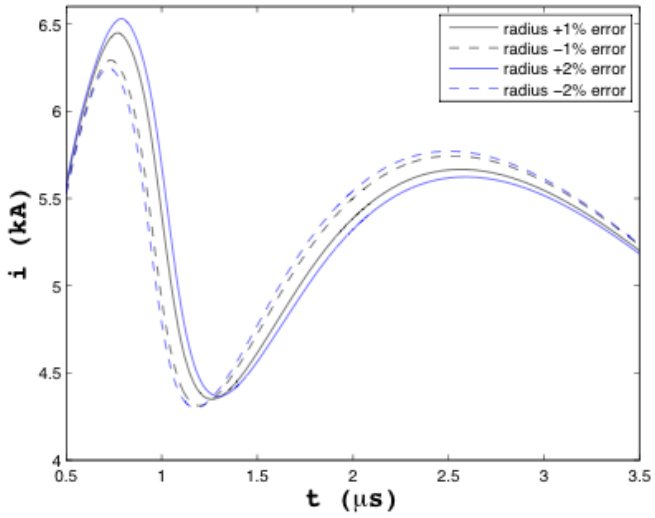

Figure 12. Effect of wire diameter measurement error.

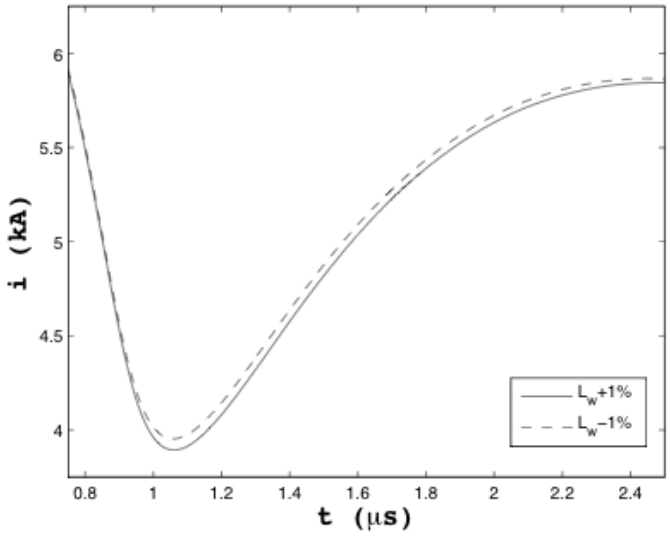

Figure 13. Effect of wire length measurement error (subregion of the current trace).

3.7.5 Electrode Thickness

Initially, we chose two very thick electrodes to minimize plate bending caused by the magnetic field and detonation. However this substantially increased the size of the mesh. We therefore investigated how thin we could make the plates without impacting the physics of the problem. The plate thickness was adjusted in multiples of ½, ¼, ⅛, and 1⁄16 of the original size. From these results (not pictured) it appeared that we could go as small as 1⁄16 of the original electrode width. However, closer inspection of the geometry revealed that the plates bent out of the mesh. While we could increase the mesh padding between the plates and the mesh boundary, we observed that ⅛ optimized the result in terms of limiting the bending and minimizing simulation time.

3.7.6 Water Conductivity Model

The conductivity of distilled water is many orders of magnitude smaller than that of the wire and electrode materials. Typical water conductivities for seawater is 5.5 S/m, tap water: 0.05–0.005 S/m, and distilled water: 10^{-5} S/m (*28*). In the latter case, however, the value is smaller than what we can use in simulations due to a numerical solver limit of about nine orders of magnitude in EC. Therefore it is important to test the effect of using a constant, small conductivity and changing its value over several orders of magnitude. Those values were chosen in multiples of an arbitrary reference value, $\sigma = 1$ S/m. Figure 14 plots the current traces for the conductivities {0.01, 0.1, 2, 10} S/m and for the scenario when the SESAME 29150 table is used. Clearly our initial value of 1 S/m was too high and the current converges as σ decreases or, equivalently, as the water acts as a better insulator. The EC of water can therefore only be modeled realistically in these simulations with the SESAME model 29150 (preferable) or a

sufficiently low constant conductivity. The latter however, may miss relevant physics in other problem geometries.

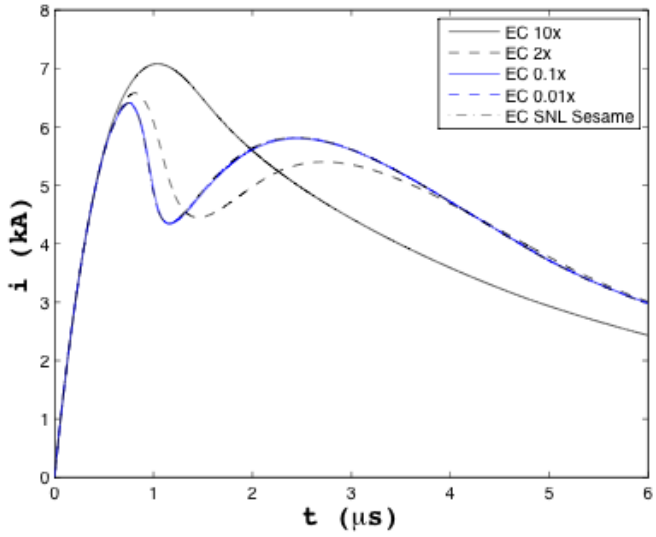

Figure 14. Current trace as a function of the water conductivity model and related settings.

3.8 Relevant Physics and Timescales

There are three mechanisms for heat transfer. Ordered by their relative timescales from slow to fast they are convection, conduction, and radiation. Convection is not relevant for this problem, and conduction is relevant to some *heated* wire problems. Radiation occurs quickly enough to be relevant, but is strongly dependent on the local temperature. Since we have the capability to include conduction and radiation in EW simulations, some discussion is needed to justify their inclusion or exclusion. For completeness, we will also examine the timescales for magnetic diffusion.

3.8.1 Thermal Conduction

The heat flux due to conduction is defined as $\boldsymbol{q} = -k\nabla T$, where $\boldsymbol{q}$ is the thermal energy Q flowing through cross sectional area A per unit time, k is the thermal conductivity and ∇T is the thermal gradient. For the present analysis, we are only interested in the radial component:

$$q_r = \frac{dQ}{dt} = -kA\frac{dT}{dr} \ . \tag{7}$$

The temperature field is determined from Laplace's equation, $\nabla^2 T = 0$ since we can presume no thermal sources. In cylindrical coordinates this becomes,

$$\frac{1}{r}\frac{d}{dr}\left(r\frac{dT}{dr}\right) = 0 \tag{8}$$

using the boundary conditions, $T(r=r_i)=T_i$, where i=1, 2, the solution of equation 8 and its spatial derivative takes the form,

$$\begin{aligned} T &= A\ln r + B \\ &= \frac{\Delta T}{\ln\left(r_2/r_1\right)}\left[\ln r - \ln r_1\right] + T_1 \end{aligned}$$

$$\frac{dT}{dr} = \frac{\Delta T}{r\ln\left(r_2/r_1\right)} \,. \tag{9}$$

Equation 7 can be solved for t using equation 9 and, along with the surface area for a cylinder, we obtain,

$$t = \frac{Q\ \ln\left(r_2/r_1\right)}{2\pi\ell k\Delta T} \,. \tag{10}$$

where ℓ is the wire length and for Al, k=237 W/(m·K). Let r_2 = 60 μm and r_1 =1 μm represent the outer and inner radii, across which the temperature gradient is applied. To thermally conduct just Q=1 J of energy across a gradient of hundreds of kelvin and a distance of about 60 μm takes a few milliseconds. For a gradient of thousands of kelvin, this decreases to hundreds of microseconds. However, at those thermal gradients the analysis begins losing validity since the Al wire has a melt temperature of only 933 K. In both cases, conduction is too slow to be relevant.

3.8.2 Thermal Radiation

To determine whether radiative heat transfer is important in the exploding wire problem we compare the energy flux radiated from a heated wire to the amount of thermal energy it receives. If we presume that the wire emits radiation as a blackbody with a constant emissivity, then the Stefán-Boltzman law applies, which states that the time rate of change of internal energy due to radiative emission is given by $dQ/dt = -\sigma_{SB}AT^4$, where A is the surface area, and σ_{SB} is the Stefán-Boltzmann constant. With wire values listed in table 1 and presuming a constant temperature of 700 K, the wire radiates at a rate of dQ/dt = –0.088 J/s. It should be noted, that this result is highly sensitive to temperature.

We may compare this rate to the power dissipated in the wire by Joule heating, which appears as thermal energy and, consequently, an increase in wire temperature (which then radiates). This rate of Ohmic (Joule) heating may be expressed as $dQ/dt = i^2R$, where $R = \ell/\sigma\pi r^2$ is the resistance and σ is the conductivity. The current is time dependent, but from experiment we know that it reaches the order of kiloamperes within hundreds of nanoseconds. If we presume a

constant current of 1 kA, then, using wire properties from table 1, the rate of Ohmic heating becomes 1 MJ/s, which dwarfs the amount due to radiation previously discussed.

We may ask the interesting question, at what temperature does the wire need to be in order for thermal radiation to be relevant? Mathematically, we can express this by forming the ratio of the magnitude of these two energy transfer rates, equating it to unity and solving for T:

$$\frac{dQ_{radiation}/dt}{dQ_{Joule}/dt} = \frac{2\pi r \ell \sigma_{SB} T^4}{i^2 \ell / \pi r^2 \sigma} = \frac{2\pi^2 r^3 \sigma \sigma_{SB} T^4}{i^2} = 1$$

$$T = \left(\frac{i^2}{2\pi^2 r^3 \sigma \sigma_{SB}} \right)^{1/4} . \tag{11}$$

With wire values listed in table 1, a temperature of approximately 20,000 K with i=1 kA would be required before emission becomes relevant. That value increases according to $T \propto \sqrt{i}$. It is also useful to investigate for what values of r and i does emission become relevant. Identically, we can check at what wire radius or magnitude of current does emission become relevant. Evaluating equation 11 with T=700 K and i=1 kA implies r=137 mm. When T=700 K and r is about 60 μm, i=1.5A.

The full representation of radiation transport is not included in ALEGRA. Only an "emission" package is available, which allows internal energy to be released locally based on a blackbody spectrum at the local temperature (*16*). This energy is lost to the calculation entirely, as absorption and scattering are excluded from this simple algorithm. Full radiation transport algorithms are available in the HEDP (high energy-density physics) version of ALEGRA, which include absorption and scattering.

In the calculations discussed up to this point, the emission algorithm in ALEGRA was used to represent radiative losses. To confirm the analysis discussed above regarding radiation, a series of computational tests was carried out for the present EW problem using the radiation diffusion algorithms in ALEGRA-HEDP. As predicted, the tests show that the contribution of radiation to the problem is insignificant. These simulations produced nearly identical behavior of the system, compared to the pure ALEGRA simulations, with both multigroup and single-group diffusion. Although the residual internal energy in the system was lower by about 2% in the radiating case, this did not affect the current or voltage traces.

Further, we also note that maximum temperatures in the simulations considered as part of this study did not generally exceed 5 eV. Therefore, following the approach of Sarkisov et al. (2005) (*13*), we incorporate only emission of radiation as a contributor to the energy balance.

3.8.3 Magnetic Diffusion

When considering common sources of error and typical magnitudes of the uncertainties in measured parameters of the experimental setup, we found that uncertainty in the wire radius, wire length, and external circuit resistance had the greatest impact on the current trace. This is previously shown in section 3.7, where we observed that sensitivity in the simulations' current trace to these parameters was greater than for other parameters such as the external circuit voltage. For appropriate comparison of simulations with the experiments, the latter of which involuntarily takes full account of such uncertainties, we therefore proceed with a series of simulations probing a three-dimensional parameter space including error bounds of ±2% in wire radius, ±5% in wire length, and ±5% in circuit resistance. We neglected any combined error in voltage, for example, since it would be within that caused by wire dimensions or resistance.

We did observe in section 3.7.6 that water conductivity can drastically impact the results. However, this effect arises only for a constant, artificially increased conductivity. Further, since only the SESAME 29150 table is available for water conductivity, we simply proceed with this model. Several of the SESAME EOS models for Al will be used and compared, but SESAME 3700 will ultimately be selected for the study and combined with uncertainty. Appendix A lists the ALEGRA input script used for our calculations.

---

4. Discussion of Simulations Compared to Experiments

The streak-camera image obtained from one of the three EW experiments described in section 2 is shown here in figure 15.

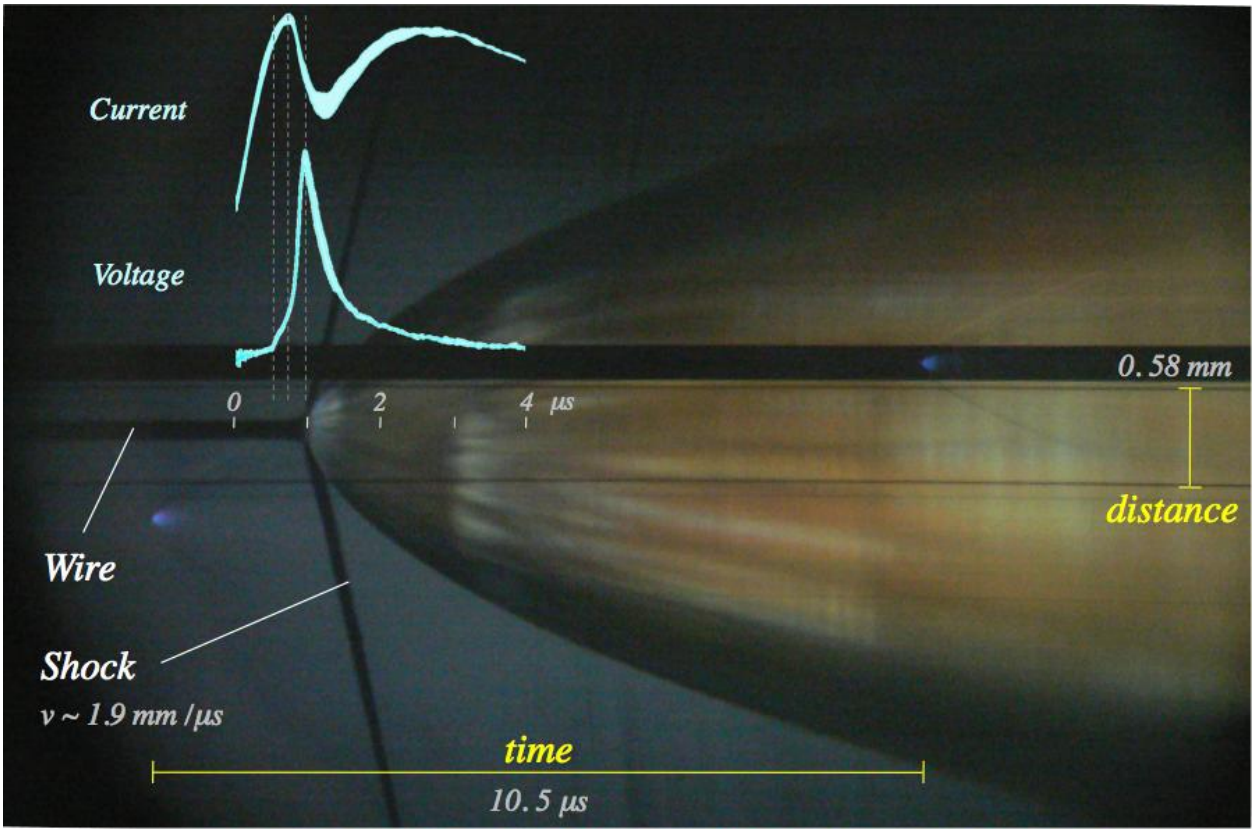

Figure 15. Streak image of a typical Al wire discharge. Timescale is determined from the two spots of blue light occurring at –1.14 μs and 9.32 μs after initiation of the discharge. The current and voltage traces from three nominally identical experiments are combined to illustrate variability and are scaled in time according to the streak image.

In this image, time increases from right to left. Recall that the streak camera observes only a small axial sliver over time. Each instantaneous view is juxtaposed with subsequent times so a single wide line (annotated as "wire" in the image) is observed as the wire's history running from left to right. Here we observe that the shock wave (annotated as "shock") propagating through the water is clearly visible running ahead of the wire expansion front, since the density gradient at the shock front strongly refracts the backlight. From our calibration, the shock speed appears to be about 1.9 mm/μs surpassing the distilled water sound speed of about 1.5 mm/μs. The plasma itself is opaque to the backlight, and is also easily seen in the streak image. It is also possible, on the original images, to distinguish a weak shock wave that precedes the main shock. This is due to the expansion that occurs as the wire passes from a solid to a liquid state. This picture demonstrates one of the great advantages of using water as a confining medium over experiments conducted in air. In water, we can observe the column diameter as a function of time, which we need to determine the plasma density and to calculate the conductivity. In air, the outer plasma boundary is poorly visible—particularly at late times—making diameter measurements inaccurate. It should also be noted that the flashlamp sparks used for time calibration are clearly visible in figure 15, as well as the blast wave fronts in air generated by the

electrical discharges between the streak camera and water chamber. These waves are visible because of the change in the refractive index of air, not because of any disturbance interior to the chamber.

Also superimposed on the streak image is the corresponding time scale with bounded and scaled voltage and current traces for all three experiments. Three faint vertical lines identify—and correlate between the two electrical traces—the melt transition, current, and voltage peaks. It is interesting that the wire/plasma amalgam becomes luminous at the voltage maximum.

4.1 Effect of Varying Material Response

Figure 16 superposes three experiments (see table 1 for parameters) and simulations using the SESAME EOS models 3700, 3711, 3720, 3721 for pure Al, and 4020 for the Al 2024 alloy. Appendix B describes these models in detail. A lavender band represents the data from these three nominally identical experiments in all subsequent plots. This band is bounded above and below by the maximum and minimum data value at each point in time from the set of three experiments. No single experiment defines any of the extrema curves. To color these bands in MATLAB, we utilized the user-contributed function `jbfill` (*29*).

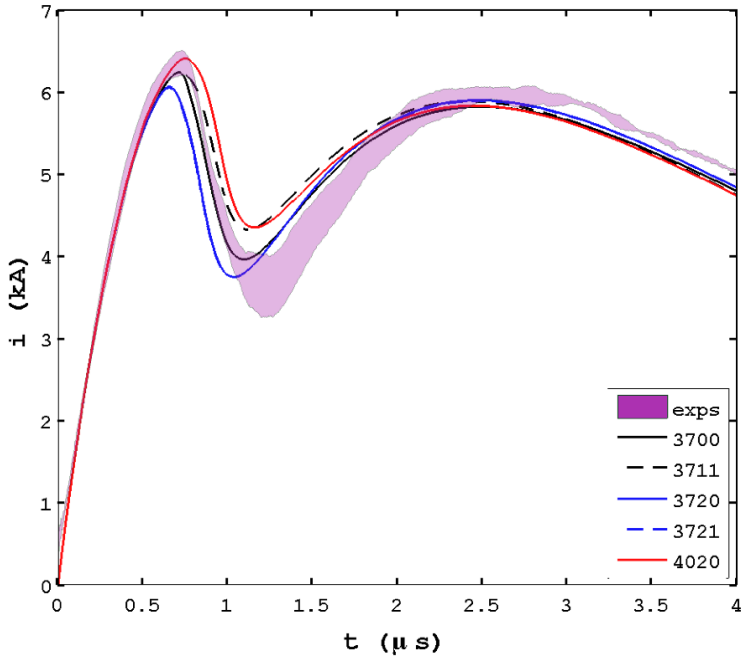

Figure 16. Current as a function of time for experiments and simulations using the Al EOS models 3700, 3711, 3720, 3721 and the Al 2024 alloy model, 4020.

In each of the simulations shown in figures 16 and 17, the Al LMD EC model was used. Results from all of the models follow the experimental trends quite well. Models 3720 and 3721 are almost identical in their response, and both fall short of the expected peak current at about 0.75 μs. We speculate that this originates with the material response rather than with details of

the geometry or circuit setup, since had appeared to only affect trends after peak current. A similar argument holds for model 3711. In this case, several of the primary parameters such as wire length or radius would have to be substantially altered to bring the trends in line with empirical results. For example, figures 12 and 13 would suggest that the radius would need to be several percent lower and length increased, respectively. Yet, the former would cause the local current minimum to occur earlier in time which is opposite of the experimental trend. It follows then that the 3700 EOS model stands as the most accurate. The Al 2024 alloy is also presented (denoted as 4020) and shows behavior similar to 3711.

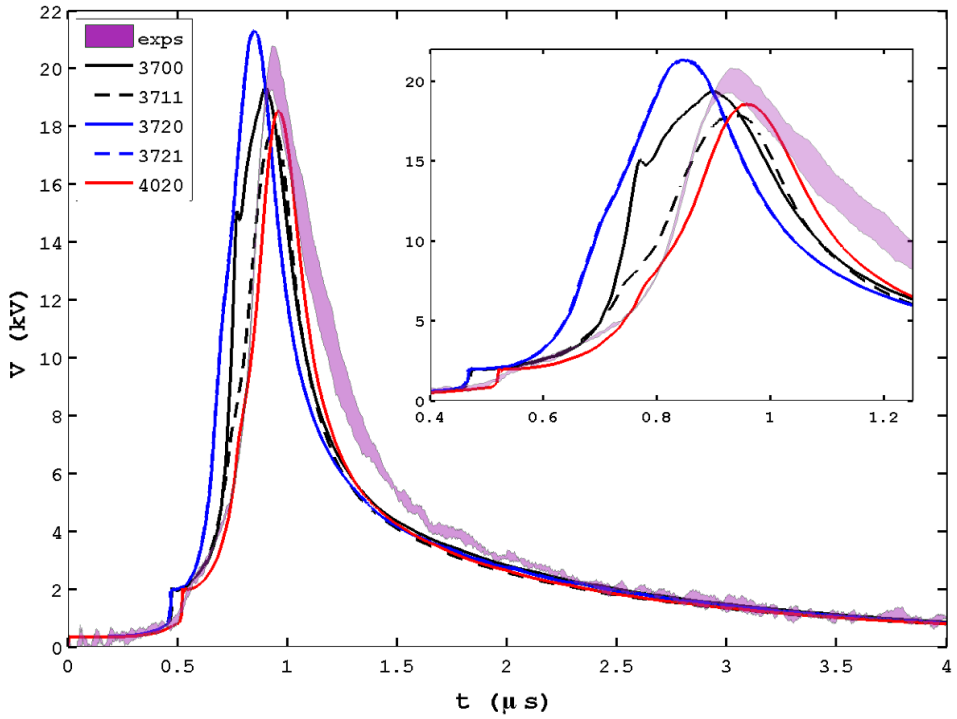

Figure 17. Voltage as a function of time for experiments and simulations using the Al EOS 3700, 3711, 3720, 3721 and the Al 6061 alloy, 4020.

Even though we are using 99.95% pure Al in the experimental component of this study, it is useful to compare the simulation results among various Al alloys. Our motivation is primarily to stress that each alloy requires its own EOS and conductivity models. However, we expect impurities to influence the conductivity much more strongly than they affect the EOS. Table 2 lists the compositions and solidus temperature for the 6061 and 7075 alloys as reported by Alcoa (*30, 31*). The solidus temperature is defined as the curve on a phase diagram below which the material is crystallized or solid. In addition, table 2 lists electrical conductivities of the impurities (*32*) normalized by that of aluminum.

Table 2. Composition and solidus temperature of the Al 6061 and 7075 alloys. The lower row tabulates the conductivity of impurities normalized by that of pure aluminum.

Alloy	Maximum Impurity Composition (% weight)										Solidus Temperature (K)
	Si	Fe	Cu	Mn	Mg	Cr	Zn	Ti	Other Total	All Total	
Al 6061	0.8	0.7	0.4	0.15	1.2	0.35	0.25	0.15	0.15	4.15	855
Al 7075	0.4	0.5	2.0	0.30	2.9	0.28	6.10	0.20	0.15	12.83	750
	6.7E-12	0.26	1.6	0.02	0.6	0.21	0.44	0.06	Conductivity of impurities normalized by that of pure Al		

Several of these alloys are available in ALEGRA's library of parameterized LMD models. Figure 18 clearly shows the electrical response sensitivity to wire composition. The plots indicate that a greater degree of impurity in the alloys results in an earlier and lower peak current compared to pure aluminum. This can be seen in the table where 7075 has about 13% of its weight in impurities while 6061 has only 4%. The normalized conductivities also listed in the table helps to illustrate the reduction in conductivity with increasing amounts of impurities. Changes in the current profile for 6061 can probably be attributed solely to the insulator Silicon. While for 7075 Silicon, Manganese, and Titanium appear to be the strongest factors. The reduced alloy conductivities leads to a deteriorated ability to hold off magnetic diffusion, Ohmic heating, phase changes, and ultimately, explosion. Even without including empirical data for the alloys, we argue that the electrical response, and no doubt the failure response, of each material demands its own model.

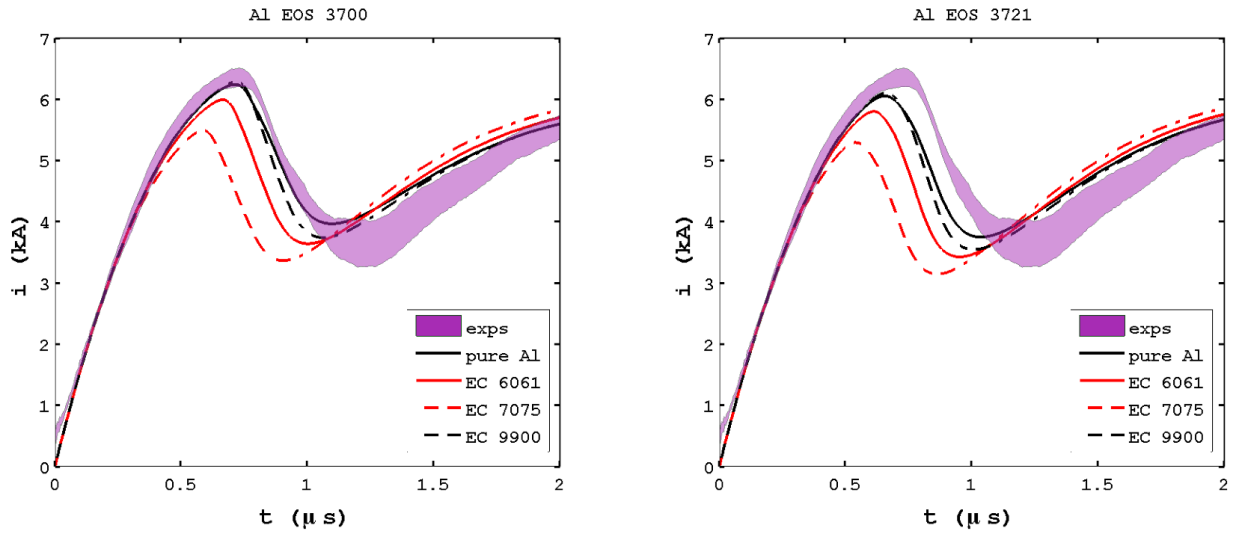

Figure 18. Current as a function of time for experiments and simulations using the Al EOS 3700 (left) and 3721 (right) with pure Al, 6061, 7075, and 9900 conductivity models.

It should be noted that the 9900 LMD conductivity model for Al consists merely of an untested prototypical set of LMD model parameters for Al, and is regarded as purely experimental. These

data are included here for the benefit of the material model developers. The simulation-experiment comparison for this conductivity model, with quantified uncertainties, is shown in appendix C.

4.2 Comparison Including Variation in Uncertain Parameters

Having examined the sensitivity of the ALEGRA solution to changes in many of the measured parameters governing the behavior of the EW system, and having also examined the effect of varying the EOS and conductivity models used to simulate the system, we now proceed to carry out the 3D parameter study described in section 3.9. This section is intended to quantify the uncertainties that are propagated to the computed result and incorporate these into the comparison of experimental and numerical results.

We begin by taking the baseline "best input" simulation—which uses SESAME 3700 and the pure-Al LMD model—and introduce uncertainties of ±5% in wire length, ±2% in wire radius, and ±5% in external circuit resistance, with respect to the mean values from table 1. This produces eight possible combinations where, at each timestep, the maximum and minimum values of the octet are determined. These extrema are plotted as the upper and lower bounds of the simulation-data band shown in figures 19 (current trace) and 20 (voltage trace). These bounds enclose results from all of the uncertainties determined from reasonable laboratory measurement errors.

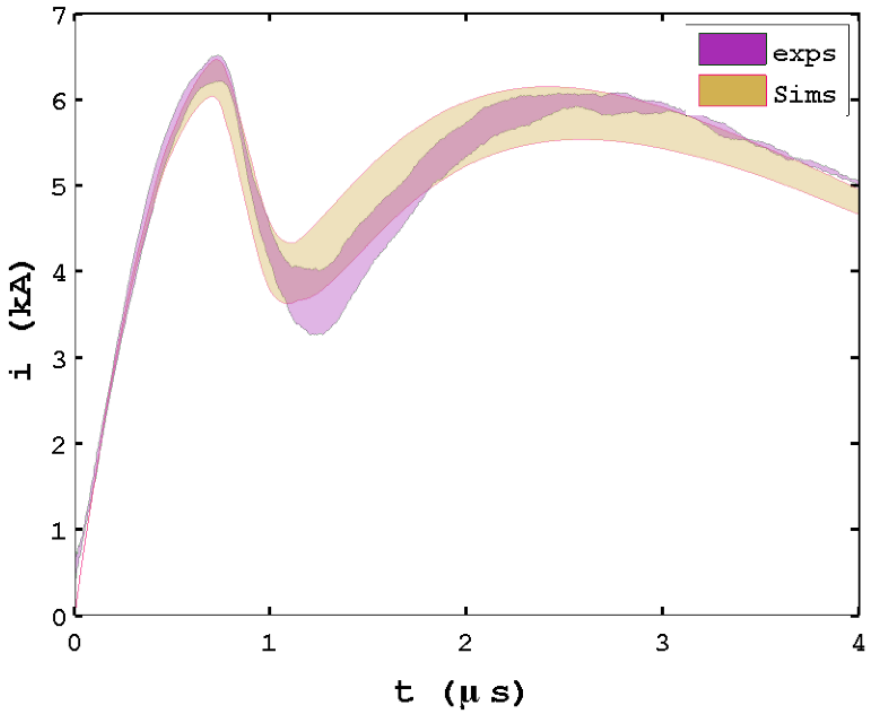

Figure 19. Current as a function of time for experiments and simulations using the Al EOS 3700 and pure Al EC, with quantified uncertainty.

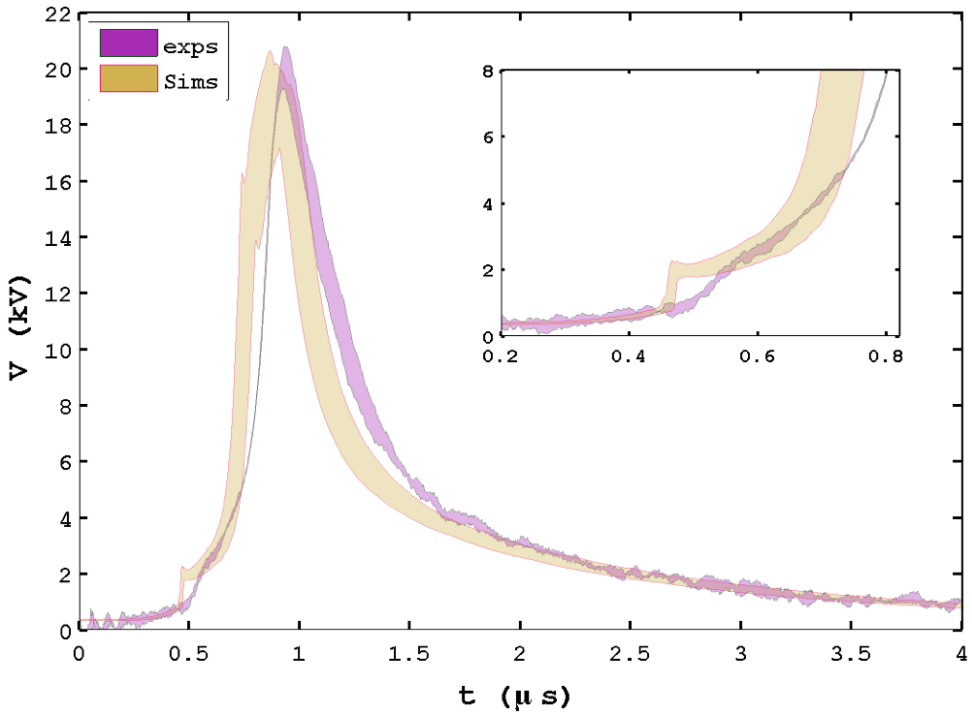

Figure 20. Voltage as a function of time for experiments and simulations using the Al EOS 3700 and pure-Al EC, with quantified uncertainty.

With the greater degree of realism afforded by quantified uncertainty, we observe in figures 19 and 20 that the extent of overlap between the two data distributions is remarkable. For the current trace shown in figure 19, the disparity between experimental and numerical results is less than the uncertainty for almost the entire 4-μs time period considered here. In fact, for most of the illustrated traces, one can easily draw a line enclosed by both experimental and computational uncertainties, which corresponds to perfect agreement. The voltage trace plotted in figure 20 appears to be much more sensitive to the details of the simulation setup and material response, as the two sets of data do diverge beyond uncertainty in several places. However, we note that the amplitude and width of the voltage pulse in time show good correspondence, though the simulated pulse occurs early by about 100 ns—10% of the time required to reach maximum voltage.

We also observe that there is some disparity in the details of the initial voltage increase at early time. As shown in the inset plot in figure 20, the simulations indicate a nearly discontinuous jump in voltage near t=0.45 μs, while the experimental data indicate a smoother increase occurring after t=0.50 μs. In the context of this study, we can say that the disparity between the voltage traces at this location must be significant, since it lies well outside the range of the uncertainties in experiment and simulation. We speculate that this sudden jump in the computed voltage originates with the transition from solid to liquid in the wire material, and the associated sudden change in density and EC. Also visible in the ALEGRA voltage trace is the presumed liquid to gas/plasma transition—betrayed by the small spike—at about 0.75 μs.

We close this study by reporting a late development yielding an improved agreement—beyond that shown in figure 19—between ALEGRA simulations and the empirical data. We find that the tail of the current trace is controlled by uncertainty in the external capacitance as figure 21 illustrates. We were prompted to look into this based on conversations with Hornbaker (*33*) who pointed out that the system may be affected by shunt capacitance which we hadn't yet considered. Just as relevant, Hummer (*34*) indicated that variability in capacitor banks can be considerable—up to 20% in some cases. Instead, we initially presumed that bank voltage would dominate over variability in capacitance. With these new physical insights, we investigated this uncertainty—whether the source was shunt or variable capacitance—and chose modest values of ±2% and ±5% about the baseline capacitance. Figure 21 plots only increases since we might expect missing capacitance. These results would push the ALEGRA results in figure 19 to higher values further strengthening the already outstanding agreement. Thus, by considering a small and realistic increase in capacitance, one can enhance correlation at late times.

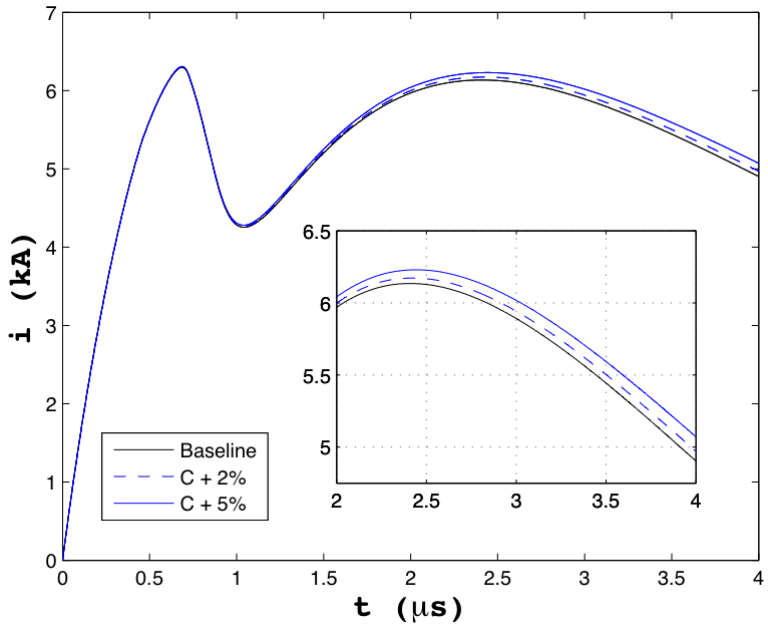

Figure 21. Current as a function of time for baseline calculations and uncertainty in the external capacitance.

5. Conclusion

In the present study, experiments and simulations were carried out in order to characterize the behavior of an exploding Al wire in a water environment, with quantified experimental and simulation uncertainties, for a single experimental setup. The convergence properties of the solution computed with ALEGRA were examined using the inductance of the system, showing that a mesh subtending 400 wire radii, with a resolution of about 3.8 elements per initial wire radius, was adequate. A sensitivity study for various inputs to the simulation—including dimensions, external circuit parameters, and material model characteristics—identified the most important uncertain parameters by examining the variation in current traces from the computed solution. These parameters were found to be the wire dimensions (length and radius), the external circuit resistance and capacitance.

A series of simulations probing the 3D parameter space defined by variations within uncertainty was carried out. The distribution of simulation results was then compared to the distribution of results from three nominally identical experiments. This comparison superposed bands of experimental and simulation data in order to compare distributions, rather than individually comparing single data points and trends. The outcome demonstrated a remarkable level of agreement between experimental and simulation results in the current history, though the voltage history exhibited some notable differences. Because quantified uncertainty was included, the degree of disparity could be quantified in a more meaningful way, based on whether it exceeded the uncertainty.

The important observations and conclusions drawn from this study include the following.

- With quantified uncertainty, the possibility is greatly reduced of obtaining a result that may at face value falsely indicate an inadequacy in modeling.
- With quantified uncertainty, a much stronger statement of the significance of experimental/numerical disparities can be derived.
- The data shown here indicate that Al is a very well characterized material for these applications, as numerical simulations using ALEGRA can predict the measured current history to within the uncertainty.
- While the overall trend is correct, certain features of the voltage history are not well predicted by the simulations. This indicates that there is still room for improvement. Results with the modified 9900 EC model (appendix C) may provide clues for doing so—particularly the melt transition at 500 ns.

We anticipate that future work in this area will help to clarify exactly what features of the material response may yield further improvements in predictive capability, e.g., the tension regime in the EOS, ionization potentials in the conductivity models, and so on. Most likely these findings would be applicable to other metal material models. Rosenthal and Desjarlais (*8*) have identified "inadequate solid binding energy . . . and inaccurate specific heat" as possible issues with the EOS. Future work will also extend our study to other materials and to other regimes of energy where the phenomenology may change.

6. References

1. Chace, W.G.; Moore, H.K. *Exploding Wires*; Vol. 1; New York: Plenum Press, Inc., 1959.
2. Chace, W.G.; Moore, H.K. *Exploding Wires*; Vol. 2; New York: Plenum Press, Inc., 1962.
3. Chace, W.G.; Moore, H.K. *Exploding Wires*; Vol. 3; New York: Plenum Press, Inc., 1964.
4. Chace, W.G.; Moore, H.K. *Exploding Wires*; Vol. 4; New York: Plenum Press, Inc., 1968.
5. Chace, W.G. Exploding Wires. *Physics Today*. **1964**, pp. 19–24.
6. Sinars, D.B; Shelkovenko, T.A.; Pikuz, S.A.; Greenly, J.B.; Hammer, D.A. Exploding aluminum wire expansion rate with 1-4.5 kA per wire. *Phys. Plasmas.* **2000**, *7* (5), 1555.
7. Chandler, K.M.; Hammer, D.A.; Sinars, D.B.; Pikuz, S.A.; Shelkovenko, T.A. *IEEE Transactions of Plasma Science* **April 2002**, *30* (2).
8. Sinars, D.B.; Hu, M.; Chandler, K.M.; Shelkovenko, T.A.; Pikuz, S.A.; Greenly, J.B.; Hammer, D.A.; Kusse, B.R. Experiments measuring the initial energy deposition, expansion rates and morpholofy of exploding wires with about 1kA/wire. *Phys. Plasmas.* **2001**, *8* (1), 216.
9. Rosenthal, S.E.; Desjarlais, M.P.; Cochrane, K.E. *Equation of State and Electron Tranport Effects in Exploding Wire Evolution*; SAND2001-1896C, 2001.
10. Degnan, J.H.; Taccetti J.M. Implosion of solid liner for compression of field reversed configuration. *IEEE Trans. Plasma Sci.* **2001**, *29*, pp. 93–98.
11. Desjarlais, M.P.; Rosenthal, S.E.; Douglas, M.R.; Cochrane, K.; Spielman, R.B.; *Mehlhorn, T.A. Study of Conductivity and EOS Variations in Exploding Wire Simulations.* GP1.066 Poster Session IV, 42nd Annual Meeting of the APS Division of Plasma Physics, Quebec City, Canada, October 23–27, 2000.
12. Mehlhorn, T.A.; Stoltz, P.H.; Haill, T.A.; Desjarlais, M.P.; Douglas, M.R. *Verification and Validation of ALEGRA-MHD on exploding wire data*. GP1.065 Poster Session IV, 42nd Annual Meeting of the APS Division of Plasma Physics, Quebec City, Canada, October 23–27, 2000.
13. Sarkisov, G.S.; Rosenthal, S.E.; Cochrane, K.R.; Struve, K.W.; Deeney, C.; McDaniel, D.H. Nanosecond electrical explosion of thin aluminum wires in a vacuum: Experimental and computational investigations. *Phys. Rev. E.* **2005**, *71*, 046404.

14. Vunni, G. B.; DeSilva, A.W. *Electrical Conductivity Measurement of Nonideal Carbon Plasma*; ARL-TR-4551; U.S. Army Research Laboratory: Aberdeen Proving Ground, MD, August, 2008.

15. DeSilva A. W.; Vunni G. B. Electrical Conductivity of Carbon Plasma. *Phys. Rev. E.* **2009** *79*.

16. Vunni, G.B.; Doney, R. L. *Experimental Investigation and ALEGRA-MHD Simulation of Electrical Explosion of Copper Wire in Air and Water*; ARL-TR-4552; U.S. Army Research Laboratory: Aberdeen Proving Ground, MD, March, 2009.

17. DeSilva, A.W.; Katsouros, J.D. Electrical conductivity of dense copper and aluminum plasmas. *Phys. Rev. E.* **1998**, *57*, 5947.

18. ALEGRA: Version 4.6, SAND2005-draft, Unlimited Release Printed Unpublished Draft, dated January 2005.

19. ALEGRA-MHD: Version 4.6, SAND2005-draft, Unlimited Release Printed Unpublished Draft, dated January 2005.

20. Robinson, A.C.; Garasi, C.J. Three-dimensional z-pinch wire array modeling with ALEGRA-HEDP. *Comp. Phys. Comm.* **2004**, *164*, (1–3), pp 408–413.

21. Robinson, A.C., et al. *ALEGRA: An Arbitrary Lagrangian-Eulerian Multimaterial, Multiphysics Code*; AIAA Paper, 2008–1235, 2008.

22. Davidson, P.A. *An Introduction to Magnetohydrodynamics*; Cambridge University Press, 2001.

23. Kovetz, A. *Electromagnetic Theory*, Oxford University Press, 2000.

24. Desjarlais, M. P. Practical Improvements to the Lee-More Conductivity Near the Metal-Insulator Transition Contributed to *Plasma Phys.* **2001**, *41* (2–3), 267–270.

25. Knoepfel, H. *Pulsed High Magnetic Fields*; Elsevier, New York, 1970.

26. Baker, L. Simulation of the burst phase of exploding wires. *J. Appl. Phys.* **1980**, *51* (3), 1439.

27. Davison, L.; Graham, R.A. Shock compression of solids. *Physics Reports*. **1979**, *55*, 255–379, table 3.6.

28. Hornbaker, D. Private communication, May 31, 2010.

29. Bockstege, J. http://www.mathworks.com/matlabcentral/fileexchange/13188-shade-area-between-two-curves (accessed 26 September 2009).

30. http://www.alcoa.com/gcfp/catalog/pdf/alcoa_alloy_6061.pdf (accessed 19 May 2010).

31. http://www.alcoa.com/gcfp/catalog/pdf/alcoa_alloy_7075.pdf (accessed 19 May 2010).

32. http://environmentalchemistry.com/yogi/periodic/electrical.html (accessed 19 May 2010).

33. Hornbaker, D. Private communication, May 31, 2010.

34. Hummer, C. Private communication, June 3, 2010.

INTENTIONALLY LEFT BLANK.

Appendix A. ALEGRA Input Script

```
$ {_FORMAT="%.10g"}
$ --- COMMENTS ---
$ B. Doney 4/23/09

$mm2m :{mm2m = 1.00e-3}

$WIRE_LENGTH:   {WIRE_LENGTH=0.0165 - 0.05*0.0165}         $ (m)
$WIRE_DIAMETER: {WIRE_DIAMETER=127.857e-6 - 0.02 * 127.857e-6}   $ (m), measured from
SEM
$WIRE_RADIUS:   {WIRE_RADIUS=WIRE_DIAMETER/2} $ (m)
$PLATE_SEP:     {PLATE_SEP=WIRE_LENGTH}       $ (m)
$PLATE_RAD:     {PLATE_RAD=WIRE_RADIUS*400}   $ (m)
$PLATE_THICK:   {PLATE_THICK=0.01/8}          $ (m)

$RESISTANCE: {RESISTANCE = 2.0 - 0.05*2.0}
$PADDING:       {PADDING=5e-4}       $ Mesh padding (m)
$ZMIN:{ZMIN = -PLATE_SEP/2.0-PLATE_THICK-PADDING}
$ZMAX:{ZMAX = PLATE_SEP/2.0+PLATE_THICK+PADDING}
$ZTOT:{ZTOT = ZMAX-ZMIN}
$RES:{RES = 60}  $ Number of elements per millimeter (was 60)
$CELL_SIZE:{CELL_SIZE = mm2m / RES}
$NUM_ELE_WIRE:{NUM_ELE_WIRE=WIRE_RADIUS/CELL_SIZE}      $ Num elements in wire

$BX:{BX = 1} $ Number of Blocks in X (R)
$BY:{BY = 1} $ Number of Blocks in Y (Z)
$NX:{NX = int(PLATE_RAD/CELL_SIZE)}
$NY:{NY = int(ZTOT/CELL_SIZE)}

$ Contact points for slot boundary condition
$BCZ0: {BCZ0 = -PLATE_SEP/2.0 - PLATE_THICK}
$BCZ1: {BCZ1 = -PLATE_SEP/2.0}
$BCZ2:       {BCZ2 = PLATE_SEP/2.0}
$BCZ3: {BCZ3 = PLATE_SEP/2.0 + PLATE_THICK}

$GMIN_X:{GMIN_X = 0.0}
$GMIN_Y:{GMIN_Y = ZMIN}
$GMAX_X:{GMAX_X = PLATE_RAD}
$GMAX_Y:{GMAX_Y = ZMAX}

$tstart:{tstart = 0.0e-6}             $ Mag start time
$tstop: {tstop  = tstart+100.0e-6}    $ Mag stop time

$ Temperature clip options (refer to sesame.ref)
$ {EOS_Tmax_Al = 1.0e5}               $ Max Temp EOS Table Al
$ {EOS_Tmax_Air= 348150016.0}         $ Max Temp EOS Table Air
$ {Tmax_Al = 1.0e4}                   $ Temp Clip Al
$ {Tmax_Air= 5.0e4}                   $ Temp Clip Air
$ {HiClip_Al = EOS_Tmax_Al - Tmax_Al} $ HiClip Al
$ {HiClip_Air= EOS_Tmax_Air-Tmax_Air} $ HiClip Air
$ {LoClip_Al = 50.0}
$ {LoClip_Air = 50.0}
${ECFloor=1.0e-2}
$$$$$$$$$$$$$$$$$$$$$$$$$$$$$$$$$$$$$$$$$$$$$$$$$$$$$$$$$$$$$$$$$$$$$$$$$$$$$$$$$$$$$$$
title: Exploding wire
```

```
units, si

termination time 6.0e-6
check shutdown file, 1m

magnetohydrodynamics
  cylindrical     $ R-Z

  void compression = off
  ignore kinematics errors
  rotation representation, quaternion
  gradual startup factor, 0.1
  time step scale, 0.95
  density floor, 1.0e-2

$ --- INLINE MESH ---
  mesh, inline
    rectilinear
      bx = {BX}
      by = {BY}
      nx = {NX}
      ny = {NY}
      gmin = {GMIN_X} {GMIN_Y}
      gmax = {GMAX_X} {GMAX_Y}
    end
    set assign
      nodeset,ilo,30
      nodeset,ihi,10
      nodeset,jlo,40
      nodeset,jhi,20
      sideset,ilo,30
      sideset,ihi,10
      sideset,jlo,40
      sideset,jhi,20
    end
  end

  $ No normal displacement on all boundaries
  no displacement, nodeset 30, r
  no displacement, nodeset 10, r

  block 1
    EULERIAN MESH
    add diatom input
  end

 domain
    NEW SMYRA INTERFACE TRACKER
  end

  $random density, block 1, range 0.005, aggregate size {CELL_SIZE*0.1}

$$$$$$$$$$$$$$$$$$$$$$$$$$$$$$$$$$$$$$$$$$$$$$$$$$$$

  transient magnetics

     start, {tstart}
     stop,  {tstop}

  $ Material-Mask ID after Circuit,
```

```
  rz cyl radial slot bc, sideset 10, circuit, MATERIAL 3, r 0., z
0.,{BCZ0},{BCZ1},{BCZ2},{BCZ3}

    circuit node 1 fixedv 0.0
    circuit node 2
    circuit node 3
    circuit node 4 startv -19.98e3

    circuit element, 1 2, mesh
    circuit element, 2 3, resistor, {RESISTANCE}
    circuit element, 3 4, inductor, 1.15e-6
    circuit element, 4 1, capacitor, 1.88e-6

    circuit solver, rel 1.e-5, abs 1.e+5

  $ Specify that current may flow into and out of the mesh along the plates. Jz=0 or
Etangent=0
  e tangent bc, sideset 10, 0.0, MATERIAL 2, r 0.0 z -1.0

  void conductivity {ECFloor}
  aztec set, 1
  joule heat, maxsigma
  magnetic force, tensor
  current tally, 1, sideset 10, end
  END   $ transient magnetics

$$$$$$$$$$$$$$$$$$$$$$$$$$$$$$$$$$$$$$$$$$$$$$$$$$
$ ---  EMISSION MODEL INPUT
emission
  blackbody
    emission energy floor = .01
    max emission density = 1.0e3
    max newton iterations = 1
    tolerance = 0.1
    minimum temperature 100.0
    group bounds   $ keV
    log 0.001 to 10. by 1
  end
end

$ --- MATERIAL INSERTION ---
diatoms

  package 'wire'
    material = 1
    numsub = 50
    insert box
      p1 = 0.0 {-PLATE_SEP/2.0}
      p2 = {WIRE_RADIUS} {PLATE_SEP/2.0}
    endinsert
  endpackage

  package 'Front_plate'
    material = 2
    insert box
      p1 = 0.0 {-PLATE_SEP/2.0}
      p2 = {PLATE_RAD} {-PLATE_SEP/2.0-PLATE_THICK}
    endinsert
  endpackage
```

```
  package 'Back_plate'
    material = 2
    insert box
      p1 = 0.0 {PLATE_SEP/2.0}
      p2 = {PLATE_RAD} {PLATE_SEP/2.0+PLATE_THICK}
    endinsert
  endpackage

  package 'Water'      $ Water in electrified space
    material = 3
    insert box
      p1 = 0 {-PLATE_SEP/2.0}
      p2 = {PLATE_RAD} {PLATE_SEP/2.0}
    endinsert
  endpackage

  package 'Air'
    material = 4
    insert box
      p1 = 0.0 {GMIN_Y}
      p2 = {PLATE_RAD} {GMAX_Y}
    endinsert
   endpackage

enddiatom

end  $ MHD

$$$$$$$$$$$$ execution control $$$$$$$$$$$$$$$$$$$$$$$$$$$$$$$$$$$$$$$$

emit output: time  = 20.0E-6, from 0. to 1.
emit plot: time interval = 4e-9
emit hisplt: time interval = 4e-9
emit restart: time interval = 1.0e-6

Plot variable
  J
  Je
  Btheta
  PSI
  density
  density, avg
  velocity
  temperature
  temperature, avg
  sound speed
  econ
  econ, avg
  pressure
  pressure, avg
end

$$$$$$$$$$$$ algorithm control $$$$$$$$$$$$$$$$$$$$$$$$$$$$$$$$$$$$$$$$
aztec 1
 solver, cg
 scaling, sym_diag
 conv norm, rhs
 tol= 1.e-8
 max iter = 10000
end
```

```
$$$$$$$$$$$$ material model control $$$$$$$$$$$$$$$$$$$$$$$$$$$$$$$$$$$$$$$$$$$
material 1 wire         $ Al Wire
  model = 100
  model = 105           $ electrical conductivity        (EC LMD)
end

model 100  cth elastic plastic
  eos model   =       120
  yield model =       130
  poissons ratio = 0.33
end

$model 120 snl sesame     $ Al EOS

model 120 keos sesame
  feos = 'sesame'
  neos = 3700
end

model 130 johnson cook ep
  matlabel = 'ALUMINUM'
end

model 105 lmd
 z=13.
 tuned aluminum
 temp cutoff = 0.001
 ec floor = {ECFloor}
end
$########################

material 2 plates       $ Aluminum plates
  model = 200           $ cth elastic plastic
  model = 205           $ electrical conductivity        (EC LMD)
end

model 200 cth elastic plastic
  eos model      = 220
  yield model    = 230
  poissons ratio = 0.33
end

model 220, keos sesame
  datafile = 'EOS_data'
  matlabel = 'ALUMINUM'
end

model 230 johnson cook ep
  matlabel = 'ALUMINUM'
end

model 205 lmd         $ Al EC
 z=13.
 tuned aluminum
 temp cutoff = 0.001
 ec floor = {ECFloor}
end
$########################
```

```
material 3 water
  model = 300           $ EOS
  model = 305           $ electrical conductivity
end

$model 300 snl sesame
model 300 keos sesame
  feos = 'sesame'
  neos = 7150
end

$model 305 ec knoepfel   $ constant conductivity
$  sigma0 = 0.01
$  alpha = 0
$  betacv = 0
$end

model 305 snl sesame     $ Al EOS
   table = 602
   nmat = 29150
   feos =
'/mnt/lustre/usrcta/unsupported/MHD/16Jun2009/matdata/SNL_Sesame/h2o29150.asc'
end
$########################

material 4 air
  model = 400           $ EOS                           (KERLEY ANEOS)
  model = 405           $ electrical conductivity       (EC LMD)
end

model 400 keos sesame             $ Air EOS
   feos = 'sesame'
   neos = 5030
   loclip = {LoClip_Air}
   hiclip = {HiClip_Air}
end

model 405 lmd
  material = 'air'
  ec floor = {ECFloor}
  temp cutoff = 0.0001
end

$########################
exit
```

Appendix B. Aluminum Equation of State Details

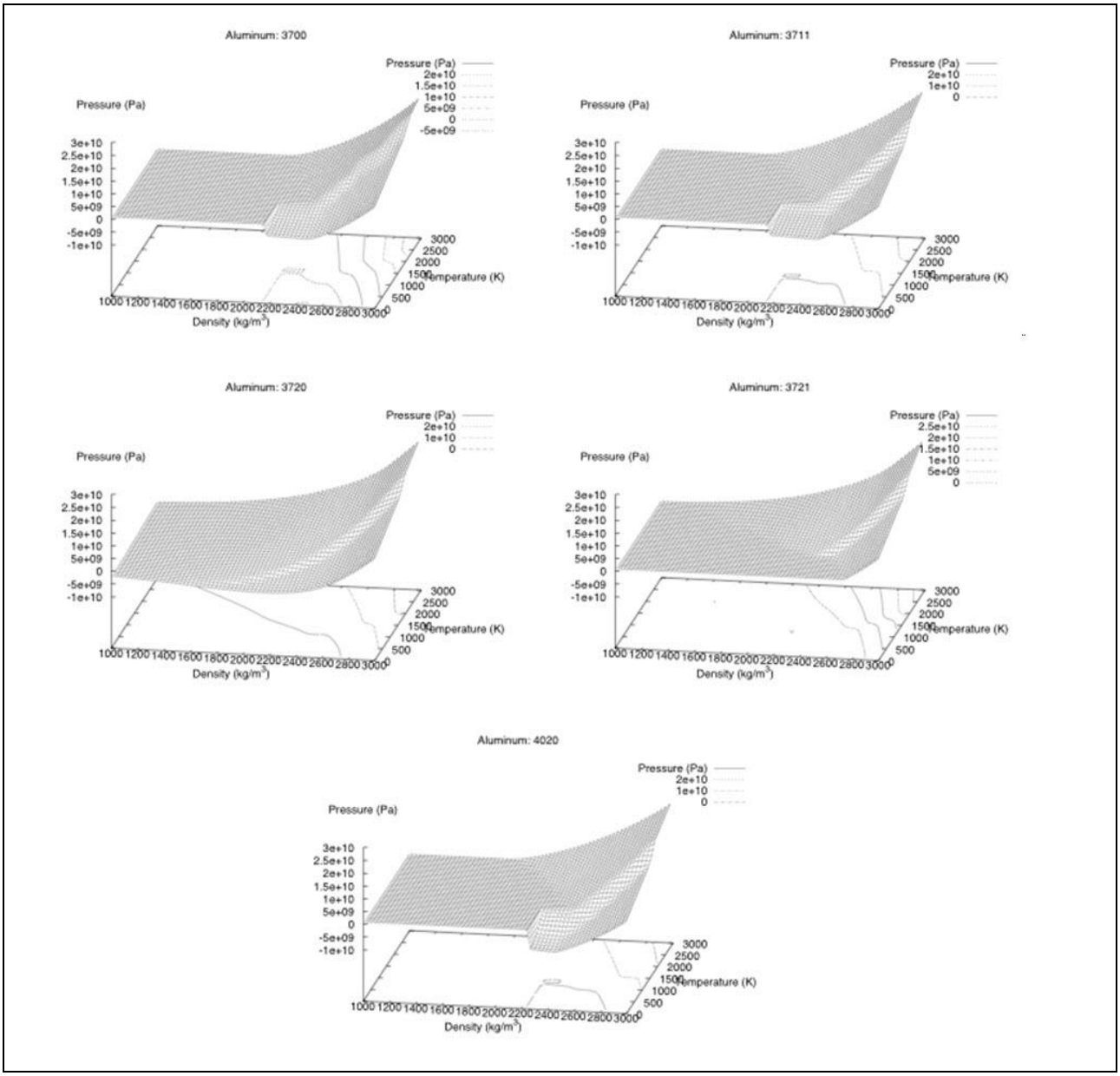

Figure B-1. EOS surfaces $p(\rho,T)$ from SESAME and ANEOS data in ALEGRA repository.

The various EOS models used in this study for Al are described here briefly, using information provided by the ALEGRA repository. Figure B-1 shows the EOS surface for each model: pressure as a function of density and internal energy density. In most cases, these models have been constructed based on theoretical principles and codes such as PANDA and GRIZZLY,

and have been calibrated to empirical data—primarily from shock wave experiments. Cochrane et al.[1] provides a helpful reference on the processes used to construct and validate models such as these, as well as the uncertainties and inconsistencies inherent to them.

B.1 SESAME 3700

The SESAME 3700 model spans 121 data points in the density range, up to 50,000 kg/m^3, and 51 data points in the temperature range, up to 10^5 K. The current model dates to 1993, but was originally built in 1986 by Kerley.[2] The model accounts for both melting and vaporization, and incorporates a tension region ($p < 0$ in the solid state) for $T < 1500$ K. The table uses Maxwell constructions inside the vapor dome to ensure stability by using pressure isotherms with $\partial p/\partial \rho = 0$. Ionization is included by use of an equilibrium model. The 3700 table is the recommended model for pure Al in the ALEGRA KEOS SESAME interface, and has been used extensively and successfully in many applications. (The KEOS format is a tabular format based on Kerley's construction.) The table is also used with a modified ambient density for many Al alloys. At ambient conditions, Al in the 3700 model has a density ρ=2699.3 kg/m^3 and sound speed c=5.2097 km/s.

B.2 ANEOS 3711

The ANEOS 3711 table contains data tabulated in SESAME format, derived from the analytic "ANEOS" models, and is called from ALEGRA using the ANEOS interface. It spans 70 density points up to 70,000 kg/m^3 and 45 temperature points up to 10^8 K. The model is credited to Trucano (no published reference) and dates to 1992. It includes solid, liquid, and gaseous phases, with tension ($p < 0$) for parts of the region where $T < 940$ K and $\rho < 2533.3$ kg/m^3. The model also uses Maxwell constructions and accounts for ionization. At ambient conditions, Al in the 3711 model has a density ρ=2700 kg/m^3 and sound speed c=5.424 km/s.

B.3 SESAME 3720 and 3721

The SESAME 3720 table contains data tabulated in SESAME format, and is called from ALEGRA using the SNL SESAME interface. It spans 111 density points up to 54,000 kg/m^3 and 77 temperature points up to 1.16×10^9 K. The model was built by Cochrane, et al.[3] (Refer to the reference in footnote 1 for a brief description.) Van der Waals loops are used in the vapor dome region of the table; thus the constraint, $\partial p/\partial \rho = 0$, may not be satisfied for states that fall inside the vapor dome, possibly leading to instabilities. However, the model maintains thermodynamic consistency to a greater degree than many other tables. At ambient conditions, Al in the 3720 model has a density ρ=2700 kg/m^3. All of this information holds true for the 3721 model as well, which is very similar to the 3720 table, except that the 3721 data are truncated so that negative pressures are not encountered; this is visible in figure B-1. In their

[1] Cochrane, K.; Desjarlais, M.; Haill, T.; Lawrence, J.; Knudson, M.; Dunham, G. *Aluminum Equation of State Validation and Verification for the ALEGRA HEDP Simulation Code*; SAND2006-1739; Sandia National Laboratories, 2006.

[2] Kerley G. I. Theoretical Equation of State for Aluminum; *Int. J. Impact Eng*., **5**, pp. 441–449, 1987.

[3] Cochrane, et al. (2006).

computational exploding wire study, Sarkisov et al. (2004)[4] used the 3721 table to model aluminum.

B.4 ANEOS 4020

The ANEOS 4020 model also contains SESAME-tabulated ANEOS data, and is credited to Thompson (no published reference), dated 1992. Very similar to the 3711 table, it spans 70 density points up to 71,000 kg/m^3 and 45 temperature points up to 10^8 K. It is intended to model the Al alloy 2024, and assumes the following composition: 93.4% Al, 4.5% Cu, 1.5% Mg, and 0.6% Mn by weight. Tension is included for T<999 K and ρ<2440 kg/m^3. The model accounts for solid, liquid, and gaseous phases, and includes Maxwell constructions and ionization. At ambient conditions, Al-2024 in the 4020 model has a density ρ=2793 kg/m^3 and sound speed c=5.1378 km/s.

[4] Sarkisov, G.S.; Struve, K.W.; McDaniel, D.H. *Phys. Plasmas*, 11, 4573 (2004).

INTENTIONALLY LEFT BLANK.

Appendix C. Results of LMD 9000 Model

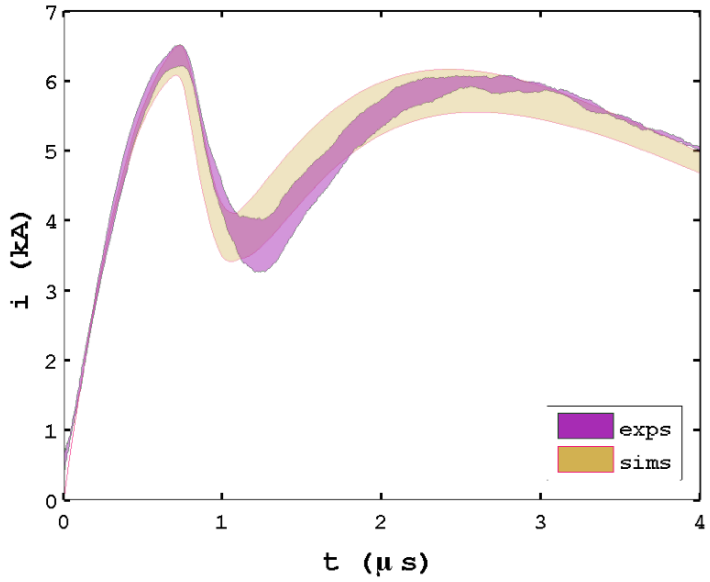

Figure C-1. Current as a function of time for experiments and simulations using the Al EOS 3700 and the LMD 9900 EC model, with quantified uncertainty.

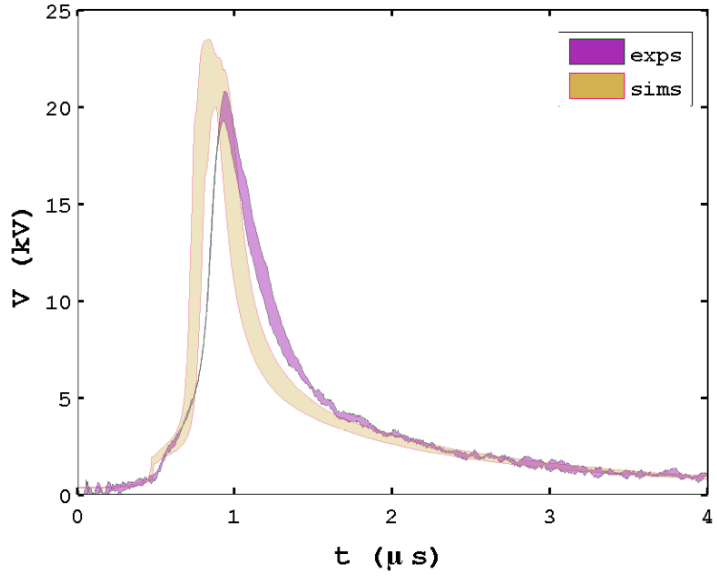

Figure C.1. Current as a function of time for experiments and simulations using the Al EOS 3700 and the LMD 9900 EC model, with quantified uncertainty.

NO. OF COPIES ORGANIZATION

1 (PDF only) DEFENSE TECHNICAL INFORMATION CTR
DTIC OCA
8725 JOHN J KINGMAN RD
STE 0944
FORT BELVOIR VA 22060-6218

1 DIRECTOR
US ARMY RESEARCH LAB
IMNE ALC HRR
2800 POWDER MILL RD
ADELPHI MD 20783-1197

1 DIRECTOR
US ARMY RESEARCH LAB
RDRL CIM L
2800 POWDER MILL RD
ADELPHI MD 20783-1197

1 DIRECTOR
US ARMY RESEARCH LAB
RDRL CIM P
2800 POWDER MILL RD
ADELPHI MD 20783-1197

1 DIRECTOR
US ARMY RESEARCH LAB
RDRL D
2800 POWDER MILL RD
ADELPHI MD 20783-1197

1 PM
JOHN ROWE (HBCT)
MS 325
WARREN MI 48397-5000

1 INSTITUTE FOR RESEARCH
IN ELECTORNICS AND APPLIED
PHYSICS
A DESILVA
ENERGY RESEARCH FACILITY
RM 1201G
UNIVERSITY OF MARYLAND
COLLEGE PARK MD 20742-3511

1 UNIV OF TEXAS AT AUSTIN
INST FOR ADVNCED TECH
SIKHANDA SATAPATHY (IAT)
3925 W BREAKER STE 400
AUSTIN TX 78759-5316

1 ROSE MCCALLEN
PO BOX 808
L-098
LIVERMORE CA 94551

NO. OF COPIES ORGANIZATION

1 SOUTHWEST RSRCH INST
ENGRG AND MAT SCI DIV
CHARLIE ANDERSON
6220 CULEBRA RD PO DRAWER 28510
SAN ANTONIO TX 78228-0610

1 SOUTHWEST RSRCH INST
ENGRG AND MAT SCI DIV
JAMES WALKER
6220 CULEBRA RD PO DRAWER 28510
SAN ANTONIO TX 78228-0610

9 SANDIA NATIONAL
LABORATORIES
MS 1189
M DESJARLAIS
T HAILL
K COCHRANE
C GARASI
MS 0378
E STRACK (3 COPIES)
M KIPP
J NIEDERHAUS
ALBUQUERQUE NM 87185

2 DEFENSE RESEARCH AGENCY
BRYN JAMES
DSTL PORTON DOWN
SALISBURY
WILTSHIRE SP4 0JQ

1 UNIVERSITY OF ALABAMA
AT BIRMINGHAM
D LITTLEFIELD
HOEN 330A
1530 3RD AVE S
BIRMINGHAM AL 35294 4440

ABERDEEN PROVING GROUND

25 DIR USARL
RDRL CIM G (BLDG 4600)
RDRL CIH C
J CAZAMIAS
RDRL WM
B FORCH
J MCCAULEY
RDRL WMP
S SCHOENFELD
P BAKER
RDRL WMP A
J POWELL
C HUMMER
C UHLIG
A PORWITZKY
P BERNING

NO. OF
COPIES ORGANIZATION

RDRL WMP B
S BILYK
R BECKER
B LOVE
J HOUSKAMP
RDRL WMP C
T BJERKE
RDRL WMP D
G VUNNI
F MURPHY
B VONK
B DONEY (3 COPIES)
RDRL WMP E
C NICELY
M LOVE
CHAMISH

INTENTIONALLY LEFT BLANK.